Draft version February 21, 2014
Preprint typeset using LaTeX style emulateapj v. 5/2/11

arXiv:1402.4818v1 [astro-ph.EP] 19 Feb 2014

MASS-RADIUS RELATIONS AND CORE-ENVELOPE DECOMPOSITIONS OF SUPER-EARTHS AND SUB-NEPTUNES

Alex R. Howe
Department of Astrophysical Sciences, Princeton University
Peyton Hall, Princeton, NJ 08544, USA and
arhowe@astro.princeton.edu

Adam Burrows
Department of Astrophysical Sciences, Princeton University
Peyton Hall, Princeton, NJ 08544, USA and
burrows@astro.princeton.edu

Wesley Verne
Department of Computer Science, Princeton University and
Princeton, NJ 08544, USA

Draft version February 21, 2014

ABSTRACT

Many exoplanets have been discovered with radii of 1−4 $R_\oplus$, between that of Earth and Neptune. A number of these are known to have densities consistent with solid compositions, while others are "sub-Neptunes" likely to have significant H_2-He envelopes. Future surveys will no doubt significantly expand these populations. In order to understand how the measured masses and radii of such planets can inform their structures and compositions, we construct models both for solid layered planets and for planets with solid cores and gaseous envelopes, exploring a range of core masses, H_2-He envelope masses, and associated envelope entropies. For planets in the super-Earth/sub-Neptune regime for which both radius and mass are measured, we estimate how each is partitioned into a solid core and gaseous envelope, associating a specific core mass and envelope mass with a given exoplanet. We perform this decomposition for both "Earth-like" rock-iron cores and pure ice cores, and find that the necessary gaseous envelope masses for this important sub-class of exoplanets must range very widely from zero to many Earth masses, even for a given core mass. This result bears importantly on exoplanet formation and envelope evaporation processes.

1. INTRODUCTION

The detection of thousands of candidate exoplanets with a wide range of masses and radii motivates the study of the general structure of planetary bodies. While early detection methods heavily favored large planets with masses and radii near those of Jupiter, the recent trend has been toward lower masses and radii, some of which appear to be terrestrial, e.g. Kepler-10b, which was recently confirmed as a planet with radius $1.416^{+0.033}_{-0.036} R_\oplus$, mass $4.56^{+1.17}_{-1.29} M_\oplus$, and average density $8.8^{+2.1}_{-2.9}$ g cm^{-3} (Batalha et al. 2011). For comparison, the average densities of the Earth and Venus are 5.5 g cm^{-3} and 5.2 g cm^{-3}, respectively.

Lopez & Fortney (2013) have suggested that it is likely that planets larger than about 1.75 $R_\oplus$ (based on mass-radius relations) have hydrogen/helium envelopes that contribute significantly to their radii. In particular, they find that a planet's radius alone provides a first-order estimate of its composition, specifically, the H_2-He mass fraction. There is some uncertainty in this limit. For example, Weiss & Marcy (2014) adopt a maximum solid planet radius of 1.5 $R_\oplus$, based in a maximum in the density distribution at ∼1.5 $R_\oplus$ and ∼7.6 $M_\oplus$ and Marcy el al. (2014b) interpret this as a transition radius of 2.0 $R_\oplus$, given an observed decrease in density from 1.5 to 2.0 $R_\oplus$.

Similarly, Rafikov (2011) suggests that envelope accretion onto a core, leading to a significant gaseous envelope, begins at a core mass of 10 $M_\oplus$, or perhaps larger if the planets form close to their stars. However, recent observations of known exoplanets suggest that envelope accretion begins, on average, at a lower mass (as found by Weiss & Marcy 2014), and some individual planets appear to acquire gaseous envelopes at very low masses. For example, Kepler-51b has been measured to have a mass of $2.1^{+1.5}_{-0.8}$ $M_\oplus$ and a radius of 7.1 ± 0.3 $R_\oplus$, corresponding to a density of $0.03^{+0.02}_{-0.01}$ g cm^{-3} (Masuda 2014b), clearly indicating a mostly gaseous composition.

Recent space-based missions such as *Kepler* (Borucki et al. 2010) and *CoRoT* (Baglin et al. 2006) had photometric precision capable of measuring transits by Earth-sized planets. In the first 16 months of the *Kepler* Mission, 207 Earth-sized ($R_p < 1.25 R_\oplus$) and 680 super-Earth-sized ($1.25 R_\oplus < R_p < 2 R_\oplus$) planetary candidates were reported (Batalha et al. 2013), suggesting a large number of solid planet candidates given a ∼1.75 $R_\oplus$ cutoff. Figure 1 provides a comparison of planets with measured radii and masses with theoretical mass-radius curves that we have generated for various simple planet compositions, including pure iron, Earth-like, Mercury-like, and pure silicate.[1] We also include on Figure 1 a

[1] We define "Earth-like" to refer to a composition of 32.5% Fe

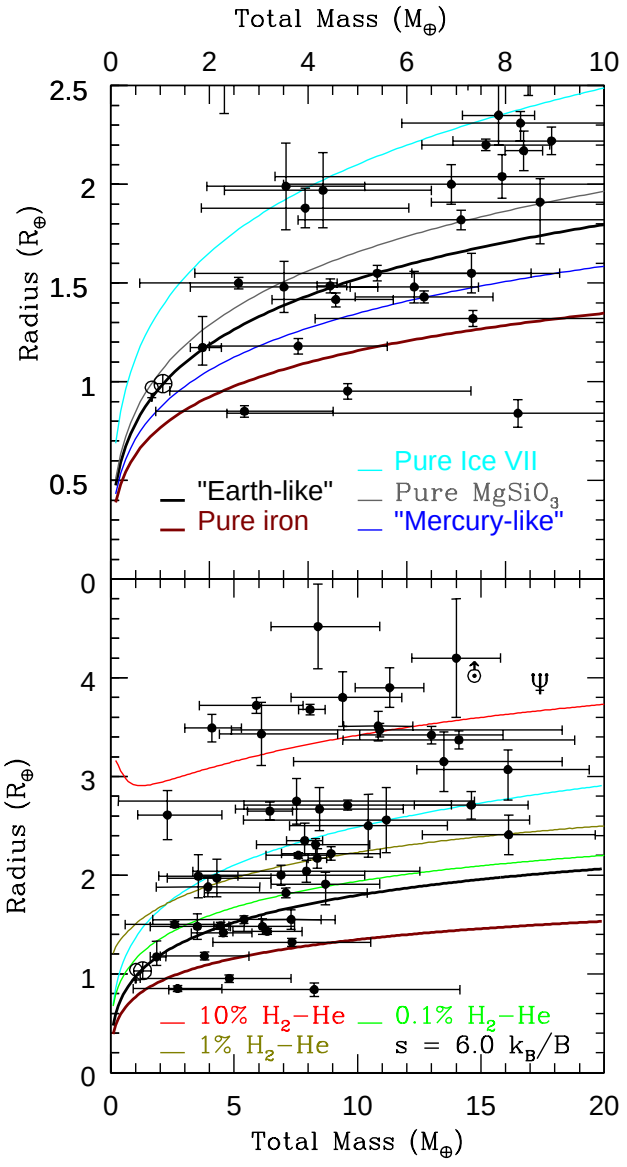

FIG. 1.— Comparison of known exoplanets and Solar System planets with our models of simple Fe core/$MgSiO_3$ mantle planets, pure water (Ice VII) planets, and planets with H_2-He envelopes. Earth-like is defined as 32.5% core mass fraction (CMF) and Mercury-like is defined as 70% CMF (Seager et al. 2007). The range of possible mass/radius values for several planets lie squarely within the area occupied by Fe core/$MgSiO_3$ mantle planets, making them excellent terrestrial exoplanet candidates. A number of others lie between the pure $MgSiO_3$ and pure Ice VII curves, making them, perhaps, candidates for "water worlds," or for possessing small H_2-He envelopes. Another population of planets at a wide range of masses is consistent only with deeper H_2-He envelopes. The measured mass and radius values and references for the plotted planets are given in Table 2.

and 67.5% $MgSiO_3$, and, when specifying a planet with a significant volatile mass fraction, a 13:27 ratio of Fe to $MgSiO_3$ mass. Similarly, we define "Mercury-like" to refer to a composition of 70% Fe and 30% $MgSiO_3$, and a 7:3 ratio if a significant volatile mass fraction is specified (Seager et al. 2007). Note, however, that recent observations from MESSENGER suggest that Mercury's iron content may be closer to 73% (Hauck et al. 2013).

pure water−in the form of Ice VII−mass-radius curve and three curves for models with gaseous envelopes: an "Earth-like" solid core and H_2-He mass fractions of 0.1%, 1%, and 10%.[2]

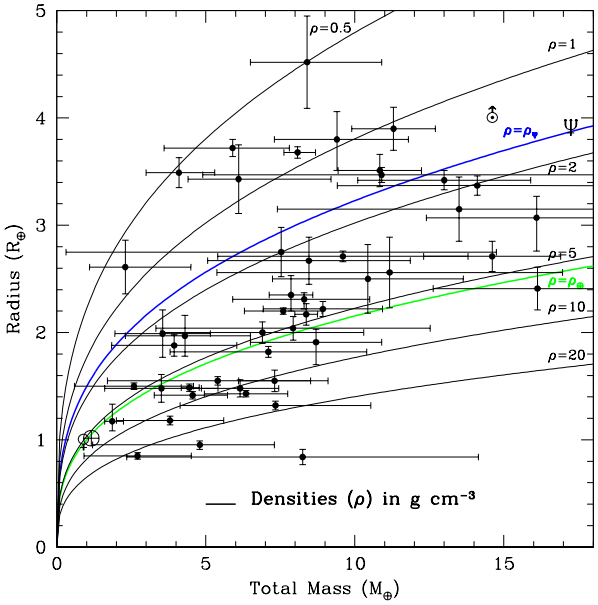

FIG. 2.— Known extrasolar planets plotted against constant density curves, including Earth's density (green) and Neptune's density (blue). Densities (ρ) are given in g cm^{-3}.

As Figure 1 demonstrates, the mass/radius values of several known planets are consistent with an iron/rocky composition, and consistent with an Earth-like composition in particular.[3] On the other hand, a number of observed planets have densities between those of pure water and pure silicate and are consistent with models of both "water-worlds" with a high water content and no significant envelopes, and models with H_2-He envelopes. Based on our models, the radius of a pure water, 10-$M_\oplus$ planet is 2.5 $R_\oplus$, which is near an observed break in the planet occurrence function in *Kepler* observations (Howard et al. 2012; Dong & Zhu 2013). However, it is not known which of these models (if either) is dominant in this radius range or whether this break reflects an actual difference in composition between planets smaller and larger than 2.5 $R_\oplus$.

In Figure 1, we note a very wide spread in the mass-radius distribution for planets more massive than ∼2 $M_\oplus$, with a variation of ∼2 $R_\oplus$ at a given mass. For planets $\lesssim$8 $M_\oplus$, this range overlaps with an Earth-like composition with no significant gaseous envelope. For higher-mass planets, some of these are also consistent with a no-envelope model if they have a sufficient water content, but we also observe planets with large radii that

[2] Throughout our paper, we use an envelope composition of 75% H_2 and 25% He by mass.

[3] One planet on the plots (Kepler-131c) has a measured density too high to be consistent with even a pure iron composition, and two others (Kepler-68c and Kepler-406c) have densities that are consistent only with the pure iron curves, likely due to the difficulty of making accurate mass measurements for smaller planets.

are consistent only with a structure that includes a deep H_2-He envelope, even at low masses ($\gtrsim$2 $M_\oplus$).

In Figure 2, we plot the extrasolar planets against constant density curves. Earth-density (green) and Neptune-density (blue) curves are included. The figure shows that density can vary by a factor of ∼5 between individual planets with the same radius. This large scatter makes it very difficult to fit any precise trends in radius with increasing mass.

In order to determine whether a given mass/radius pair indicates a solid composition, however, solid planet models and models of planets with gaseous envelopes must be constructed and compared with the data. These exoplanets may potentially have a wide range of possible compositions and temperatures and a similarly wide range of possible gaseous envelopes, so models must be able to be adjusted accordingly. Solid exoplanet models are important in both cases, since they may be used to model solid cores of planets with gaseous envelopes by applying a non-zero-pressure boundary condition at the core-envelope interface.

While there is a rich history of exoplanet structural modeling, there are a number of important areas which have yet to be investigated. For planets with gaseous envelopes, the effects of irradiation and atmospheric heating are poorly understood, and the degeneracies of envelope mass, envelope entropy, and core mass have not been explored in detail. Moreover, the implications of the large scatter in the mass-radius distribution, particularly on the search for Earth-like planets, are only beginning to be addressed.

For solid planets, equations of state for planetary materials at the pressures found in planets are subject to a degree of uncertainty, and different EOS models produce different results, which warrant analysis of the uncertainty in the modeled mass and radius values.

Our paper investigates the uncertainties and degeneracies in exoplanet modeling, particularly of planets with H_2-He envelopes, in order to gain a better understanding of what is measurable in observed exoplanets. We compute mass-radius curves over the range of 0.1 to 20 $M_\oplus$ for a variety of planet attributes, and explore the possibility of determining a precise core-envelope decomposition from mass and radius observations. We study planets with both "Earth-like" cores and ice cores, which may both be of interest depending on whether planets with gaseous envelopes form beyond the snow line. We also compute mass-radius curves for various compositional profiles for solid planets. Note that observations suggest that planets more massive than $\sim 4-8$ $M_\oplus$ are likely to possess significant H_2-He envelopes (Weiss & Marcy 2014), and the same is expected to be true of planets with radii larger than 1.5−2.0 $R_\oplus$ (Lopez & Fortney 2013; Weiss & Marcy 2014; Marcy el al. 2014b), so our results for purely solid planets likely apply only to smaller and less massive objects. Conversely, our results for planets with H_2-He envelopes will apply to planets larger than $\sim 4-8$ $M_\oplus$ or 1.5−2.0 $R_\oplus$.

Section 2 summarizes the previous work modeling solid exoplanets and sub-Neptunes. Section 3 presents our models with H_2-He envelopes and the effect on radius of varying the core mass, envelope mass, and entropy in the envelope. In Section 4, we explore the core-envelope decomposition and produce a fit to the mass-radius relation of Weiss & Marcy (2014). Section 5 demonstrates our code's output with density-pressure profiles of planets, central pressures and densities, and envelope base pressures. Section 6 presents our models of solid planets, and Section 7 sumarizes our overall conclusions. Our modeling procedure, associated code, and our studies and selection of our equations of state are described in the Appendix.

2. PREVIOUS WORK ON SOLID EXOPLANETS AND SUB-NEPTUNES

Early efforts to calculate mass-radius relationships for planetary bodies of various compositions were made by Zapolsky & Salpeter (1969), using a Thomas-Fermi-Dirac equation of state (TFD EOS) described in Salpeter & Zapolsky (1967). Those authors integrated the equations of hydrostatic equilibrium in conjunction with their EOS and a zero-pressure surface boundary condition to construct planetary structural models. This is the standard procedure for solid planet modeling; most recent advances have been in the accuracy of the low-pressure EOS, driven by the availability of experimental pressure/density data (Anderson et al. 2001).

The TFD EOS is valid only in the high-pressure limit where electrons are a non-interacting degenerate gas, but Salpeter & Zapolsky (1967) used a correlation energy correction to account for interactions between the electrons at lower pressures. They thereby extended the validity of their EOS down to ∼1 Mbar (by their estimation). However, as the TFD EOS does not account for chemical structure, it has zero-pressure density errors up to a factor of 2 (Zapolsky & Salpeter 1969). As such, Zapolsky & Salpeter (1969) focused on high-mass planets whose internal pressures lay largely in the $\gtrsim$1 Mbar regime, calculating a "critical mass" for various compositions beyond which a planet's radius decreases with additional mass. They investigated only simple monatomic elemental compositions (pure H, He, C, Mg, Fe, and various H/He mixtures) because these are most easily modeled by the TFD EOS, which considers each element separately (Salpeter & Zapolsky 1967). In addition, Zapolsky & Salpeter (1969) derived the maximum radius, and the mass and central pressure at which the maximum radius is achieved, as a function of He ratio in a H_2-He planet. Their models assumed a constant composition throughout the planet with no core-mantle-envelope differentiation, which limits their applicability for solid exoplanets.

More recent work implements equations of state based on experimental data. An early example of this approach is Stevenson (1982), who used contemporary shock wave data as the basis for his low-pressure equations of state for ices (H_2O, CH_4, and NH_3). Stevenson (1982) also investigated the interior structure and composition of giant planets, and produced mass-radius diagrams for various compositions. He reported a lack of accurate equations of state available for ferromagnesian rock, and as such, solid planet models were outside of the scope of his paper.

In the last decade, a number of authors have presented models of solid exoplanets, motivated by the aforementioned exoplanet detections, as well as the increased availability of valid semi-empirical models for terrestrial materials. Valencia et al. (2006) defined and modeled two exoplanet classes: "super-Earths," with similar compositions to Earth and planet mass 1 $M_\oplus < M_p < 10$

$M_\oplus$, and "super-Mercuries," with similar compositions to Mercury and planet mass 1 $M_{Mercury} < M_p < 10$ $M_{Mercury}$. It should be noted, however, that the term "super-Earth" is now often used to refer to any "terrestrial" planet with a mass greater than that of Earth, as well as planets in the 1−10 $M_\oplus$ range (Haghighipour 2011), or the 1.25−2.0 $R_\oplus$ range (Batalha et al. 2013). The models of Valencia et al. (2006), along with many other contemporary models (Sotin et al. 2007; Seager et al. 2007; Fortney et al. 2007), used a fourth-order Runge-Kutta integration scheme to solve the equations of hydrostatic equilibrium. The equations of state used by Valencia et al. (2006) were zero-temperature Birch-Murnaghan (B-M) equations of state (Poirier 2000) with thermal corrections using a Debye model. The B-M EOS is based on low-temperature pressure/density data. Because there are limits to the pressures that such experiments can reach, the B-M EOS incorporates an extrapolation to higher pressures. Though the thermal corrections to the equations of state for rocky materials are generally small, the model of Valencia et al. (2006) required a detailed temperature profile in order to calculate the phase transitions in the silicate mantle. Their thermal model relies on the assumption of convective heat transport in the core and mantle, with conductive layers at the core-mantle boundary and the surface. They iterated their model, using the compositional profile to determine parameters to compute the temperature profile, which was used in turn to determine phase transitions for the compositional profile calculation, until a self-consistent planet model was achieved.

Valencia et al. (2007a) applied this model to the exoplanet GJ 876d and introduced a water layer consisting of high-pressure ices covered by a thin liquid water ocean. They also used a Vinet EOS fit (Vinet et al. 1989), as opposed to the B-M EOS used by Valencia et al. (2006), because the Vinet fit is reported to extrapolate better to high pressures (Hama & Suito 1996). The model from Valencia et al. (2006) was also applied in Valencia et al. (2007b) to investigate degeneracies in the iron core, silicate mantle, and H_2O mass fractions for a given planet mass and radius and to construct ternary diagrams showing curves of constant radius for a given mass.

Sotin et al. (2007) used a similar physical approach to that of Valencia et al. (2006), but employed the stellar composition (minus H_2 and He) of the planet in constructing structural models. This approach is justified by observations that meteorite chemical ratios (thought to be representative of early planets) are similar to those found in the Sun. They used five independent parameters to determine the composition and internal structure of the planet: Mg/Si, Fe/Si, Mg# (defined as the mole fraction Mg/(Mg + Fe) in silicates), H_2O mass fraction, and total mass. They also determined a mass-radius model for planets with a water ocean.

Seager et al. (2007) conducted a broader investigation of solid exoplanets by using a simpler zero-temperature model that incorporated the Thomas-Fermi-Dirac EOS at high pressures with the Vinet semi-empirical EOS at lower pressures. They did not address phase transitions in the silicate mantle because phase transitions have little effect on the mass-radius curve of a given material and require a temperature profile. Instead, they assumed a constant-composition $MgSiO_3$ (perovskite) mantle[4]. These simplifications allowed them to investigate a wide range of planet compositions and masses.

Fortney et al. (2007) took an even broader approach, investigating five orders of magnitude in mass (0.01 Earth masses to 10 Jupiter masses) and a variety of planetary compositions, as well as envelopes. For the solid components of their planets, they used a model similar to that of Seager et al. (2007), though they used Mg_2SiO_4 (olivine) for the mantle instead of $MgSiO_3$ (perovskite), and used tabular EOS data from the ANEOS (Thompson 1990) and SESAME (Lyon & Johnson 1992) compilations, as opposed to semi-empirical fits. They neglected thermal corrections for the Mg_2SiO_4 (olivine) and iron equations of state, but for water they used a thermal EOS correction of the form

$$P = P_0 + 3.59 \times 10^{-5} \rho T, \quad (1)$$

where P is the corrected pressure in Mbar, P_0 is the zero-temperature pressure in Mbar, ρ is the density in g cm^{-3}, and T is the temperature in Kelvin. Their main goal was to produce a general, if very approximate, theory for comparison with observational data, and as such they neglected the details found in some previous papers.

Grasset et al. (2009) extended the work of Sotin et al. (2007) to masses of 100 $M_\oplus$ and also compared it with contemporary models to determine how precisely planetary compositions can be determined from mass and radius data, in particular, the water mass fraction. They found that, given uncertainties in internal structure, the water fraction can be determined with a standard deviation of 4.5% if the mass and radius are known exactly, but this uncertainty increases rapidly with the uncertainty in the radius.

Rogers et al. (2011) also investigated planets with significant H_2-He envelopes in the context of estimating plausible masses of *Kepler* planet candidates of radius 2−6 $R_\oplus$. They considered planet models with up to four layers: iron, silicates, water, and a hydrogen-helium envelope. They defined the exterior boundary condition as the radius at which the radial optical depth of the atmosphere is $\tau_R = 2/3$. They used the same EOS as Seager et al. (2007) for the solid components and the tabular EOS of Saumon et al. (1995) for the gaseous envelopes. They computed a temperature profile based on radiative transfer and radiative diffusion in the outer part of the envelope, transitioning to an adiabatic profile at the onset of convection. They considered planets produced by simulations of both core-nucleated accretion and outgassing of volatiles, particularly hydrogen. In the case of core-nucleated accretion, they considered cores of 10% iron, 23% silicates ($Fe_{0.1}Mg_{0.9}SiO_3$), and 67% water and solar-composition envelopes. They computed mass-radius curves for models with envelope mass fractions from 0.001 to 0.5, characteristic specific powers from $10^{-12.5}$ to $10^{-9.5}$ W kg^{-1}, and equilibrium temperatures of 500 K and 1000 K. For outgassing-produced envelopes, they modeled the reaction of water with iron (which produces a pure hydrogen atmosphere) on planets with water mass fractions from 8.6% to 20%.

[4] In our paper, (perovskite) or (olivine), placed after a chemical formula, refers to the crystal structure, not the specific compound or precise chemical make-up.

TABLE 1
Equations of State Used in Recent Super-Earth Modeling Papers

Authors	Material	EOS	References
Valencia et al. (2006)	Fe; FeO; Fe+alloy; $(Mg_{1-x}, Fe_x)_2SiO_4$ (olivine, wadsleyite, ringwoodite); $(Mg_{1-x}; Fe_x)SiO_3$ perovskite; $(Mg_{1-x}, Fe_x)O$	3rd order B-M, with Debye correction	1,2,3,4
Valencia et al. (2007a)	Same as Valencia et al. (2006), plus H_2O (ice)	Vinet, with Debye correction	2,3,5,6,7,8
	H_2O (liquid)	Rankine-Hugoniot	9
Fortney et al. (2007)	H_2O, olivine	ANEOS	10
	iron	SESAME 2140	11
	H_2-He	Saumon et al. (1995)	12
Sotin et al. (2007)	Same as Valencia et al. (2007a) (but different H_2O [liquid] EOS)	3rd order B-M	2,6,13,14, 15,16,17,18
Grasset et al. (2009)	H_2O (liquid)	2nd order B-M	19
Seager et al. (2007)	C (graphite); Fe (α); FeS; H_2O (ice VII); MgO; $MgSiO_3$ (enstatite); [Mg,Fe]SiO_3 (perovskite); SiC	3rd order B-M	5,15,20,21, 22,23,24, 25,26
	Fe (ϵ)	Vinet	27
	H_2O (liquid)	logarithmic EOS	28
	H_2O (VII−X transition)	tabular DFT calculations	29
	All (high pressure)	Thomas-Fermi-Dirac (TFD)	30
Rogers et al. (2011)	Same as Valencia et al. (2006)	Same as Valencia et al. (2006)	5,15,20-30
	H_2-He	Saumon et al. (1995)	12

References. — (1) Lin et al. (2003); (2) Uchida et al. (2001); (3) Williams & Knittle (1997); (4) Anderson & Isaak (2000); (5) Hemley et al. (1987); (6) Fei et al. (1993); (7) Stixrude & Lithgow-Bertelloni (2005); (8) Tsuchiya et al. (2004); (9) Stewart & Ahrens (2005), gives constraints based on shock data; (10) Thompson (1990); (11) Lyon & Johnson (1992); (12) Saumon et al. (1995); (13) Kavner et al. (2001); (14) Hemley et al. (1992); (15) Duffy et al. (1995); (16) Bouhifd et al. (1996); (17) Vacher et al. (1998); (18) Anderson et al. (1991); (19) Lide (2005); (20) Ahrens (2000); (21) Hanfland et al. (1989); (22) Zhao & Spain (1989); (23) King & Prewitt (1982); (24) Olinger (1977); (25) Knittle & Jeanloz (1987); (26) Aleksandrov et al. (1989); (27) Anderson et al. (2001); (28) Halliday et al. (2003); (29) Density functional theory calculations by Seager et al. (2007); (30) Salpeter & Zapolsky (1967).

A summary of the equations of state used in previous models of solid exoplanet structure is given in Table 1.

3. PLANETS WITH H_2-He ENVELOPES

We now present new models of planets with H_2-He envelopes with both "Earth-like" rock-iron cores with 32.5% Fe and 67.5% $MgSiO_3$ (perovskite) and with pure water (Ice VII) cores. Ice cores are of particular interest because it may be the case that planets with significant gaseous envelopes and core masses form only beyond the snow line. We compute models with varying envelope masses from 0 to 10 $M_\oplus$ and envelope entropies ranging from 5.5 to 6.5 k_B per baryon (k_B/B)−in most cases, using discrete values of 5.5, 6.0, and 6.5 k_B per baryon.[5] These values are comparable to the entropies found by the evolutionary models of Lopez & Fortney (2013) for planets of Gyr age or older.

In Figure 3, we plot radius versus total mass for planets with Earth-like cores and H_2-He envelope with mass fractions ranging from 0.01% to 20%. The code produces results consistent with the known properties of Uranus and Neptune (∼10% H_2-He) and also reproduces the upturn in radius at low masses for envelopes comprising $\geq$ 5% of the total mass, which was produced by Rogers et al. (2011).[6] Figure 3 also shows that the mass-radius curves are only slowly-rising for total masses $\gtrsim$5 $M_\oplus$, i.e. radius is not strongly dependent on total mass, while it is more strongly dependent on the mass fraction and entropy in the H_2-He envelope.

Alternatively, in Figure 4, we plot radius versus *core* mass, rather than *total* mass, for constant envelope masses of 0.01, 0.1, and 1.0 $M_\oplus$. Here, we see that for lower-mass cores ($\lesssim$5 $M_\oplus$), the planetary radius is quite sensitive to core mass and entropy, but for higher-mass cores ($\gtrsim$5 $M_\oplus$), which cover most current planet observations, the radius is most sensitive to envelope mass alone and varies very little with core mass, even less than with total mass. This suggests that mass-radius observations can be used to determine the core-envelope decomposition for a planet more precisely than the envelope mass fraction. In particular, because mass measurements usually have much larger uncertainties than radius measurements, it will be possible in many cases to determine envelope mass with more precision than mass fraction, which will have useful applications in formation models. In Table 5, we provide a sample table of properties of these models as a function of M_c for M_{env} = 0.1 $M_\oplus$ and $s = 6.0 k_B$ per baryon.

For comparison, in the top panel of Figure 5, we plot radius versus *envelope* mass for models with constant core masses of 1, 2, 5, and 10 $M_\oplus$. Here, again, we see

[5] We assume a convective envelope with constant entropy throughout. This entropy results from cooling and is a function of, among other things, age and metallicity.

[6] For these compositions, the mass corresponding to the minimum radius on the mass-radius curves increases with H_2-He fractions and increases even faster with entropy, rising from < 0.1 $M_\oplus$ for 5% H_2-He and $s = 5.5 k_B/B$ (if, indeed, there is a local minimum) to 5.5 $M_\oplus$ for 20% H_2-He and $s = 6.5 k_B/B$, among the models we study.

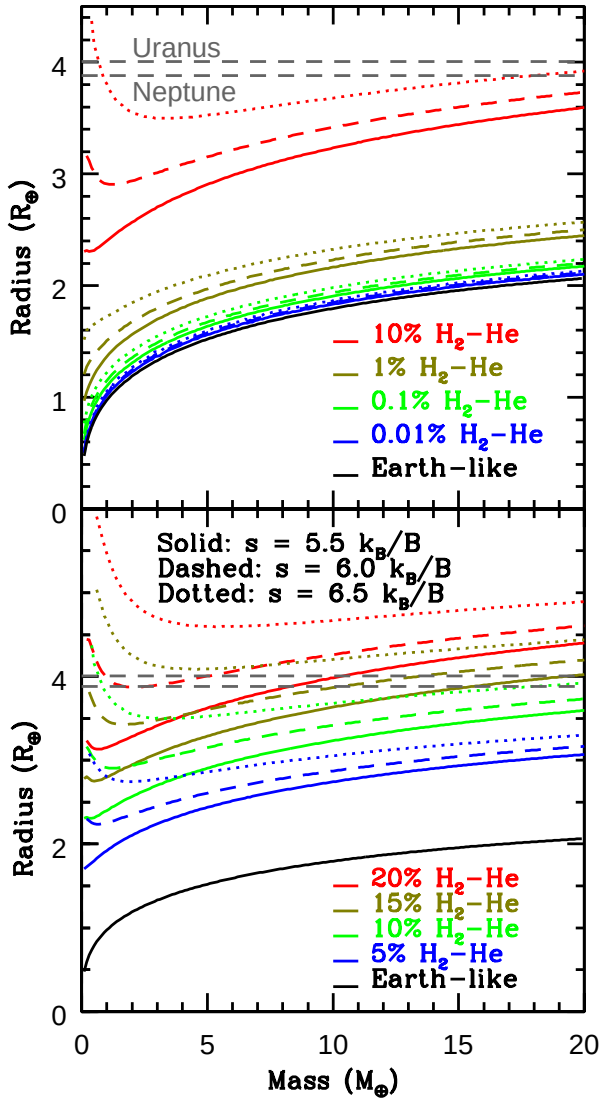

FIG. 3.— Mass-radius curves of planets with Earth-like cores and gaseous envelopes. Top panel: envelopes equal to 0.01%, 0.1%, 1%, and 10% of the total mass. Bottom panel: envelopes equal to 5%, 10%, 15%, and 20% of the total mass. Curves with envelope entropies of 5.5, 6.0, and 6.5 k_B per baryon (k_B/B) are plotted (assuming a convective envelope). An upturn in radius at low mass is apparent for larger envelope fractions. In the most extreme case of 20% H_2-He and $s = 6.5 k_B/B$, the minimum radius occurs at a mass of 5.5 $M_\oplus$. The radii are very sensitive to the H_2-He fraction, but much less sensitive to the total mass of the planet, particularly for masses > 5 $M_\oplus$.

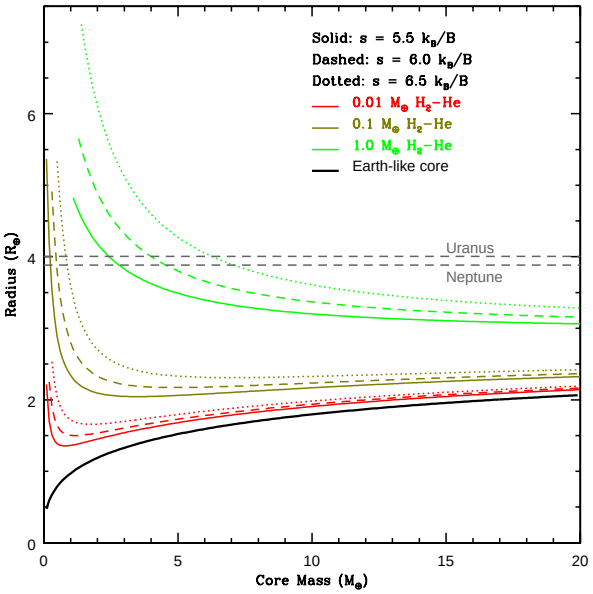

FIG. 4.— Radius versus core mass for planets with constant envelope masses of 0.01, 0.1, and 1.0 $M_\oplus$. Curves with envelope entropies of 5.5, 6.0, and 6.5 k_B/B are plotted. The curves are remarkably flat for core masses greater than $\sim$5 $M_\oplus$, indicating that the properties of the core have little influence on the observable properties of all but the smallest known planets.

that for lower-mass cores (1 and 2 $M_\oplus$), the planetary radius is quite sensitive to core mass and envelope entropy, but, for higher-mass cores (5 and 10 $M_\oplus$), radius is most sensitive to envelope mass.

We also note that the curves are relatively flat for envelopes with masses $\lesssim$0.1 $M_\oplus$, in which case the radius of the solid core dominates the total radius. However, we see another useful relation in the bottom panel of Figure 5, where we plot the envelope depth, $\Delta R = R_p - R_c$, versus envelope mass. In all cases, the envelope depth follows an approximate power law with core mass and envelope mass: $\Delta R \propto M_{env}^x M_c^y$. While the curves are bent to a slightly shallower slope at both low and high masses, the power-law indices over most of their lengths fall within a narrow range for x, $x = 0.523 \rightarrow 0.577$, but a wider range for y, $y = -0.565 \rightarrow -0.693$. We provide tables of the properties of representative models from this plot in Tables 6-10.

In Figure 6, we plot radius versus envelope mass for models with a constant core mass, 10 $M_\oplus$, and entropy, $s = 6.0\, k_B$ per baryon, but varying water fraction in the−using a core structure with iron and silicate layers surrounded by a water (Ice VII) layer, comprision a varying fraction of the core mass from no water content to a pure ice core. The effect of the water fraction on radius is dominant in planets with small gaseous envelopes of $\lesssim$ 1 $M_\oplus$. For larger envelopes, the envelope mass becomes more important, and the variation with water fraction shrinks. Changing the water abundance of the core causes the total radius of the planet to vary by up to about 30% if the envelope mass is small (so the effect of the change in the core radius is strong), but by only about 10% for larger envelopes, $M_{env} \rightarrow 10$ $M_\oplus$, less than the effect of varying the entropy for envelopes of these masses.

In Figure 7, we set constant core masses of 5 and 10 $M_\oplus$ and plot radius versus entropy for constant envelope masses of 0.01, 0.1, and 1.0 $M_\oplus$. The radius is relatively insensitive to entropy for the lower envelope masses, but entropy becomes significant for envelopes with masses $\gtrsim$1 $M_\oplus$.

4. FITS TO KNOWN PLANETS

Weiss & Marcy (2014) fit a two-piece mass-radius function to 65 low-mass planets with radii ≤ 4 $R_\oplus$ and masses measured by Marcy et al. (2014a). For planets with radii

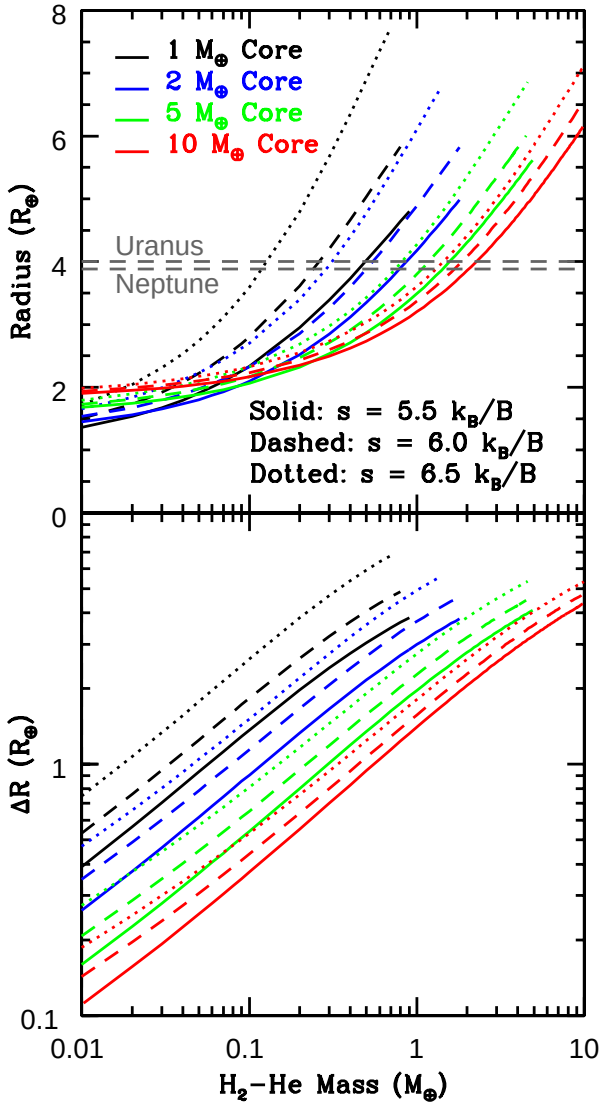

FIG. 5.— Top panel: radius versus envelope mass for planets with constant core masses of 1, 2, 5, and 10 $M_\oplus$. Bottom panel: Envelope depth ($\Delta R = R_p - R_c$) versus envelope mass. Curves with entropies of 5.5, 6.0, and 6.5 k_B/B are plotted. Envelope depth follows a power law in terms of envelope mass, $\Delta R \propto M_{env}^x$, where $x = 0.523 - 0.577$.

< 1.5 $R_\oplus$, they fit an Earth-like model defined by the density formula $\rho = 2.43 + 3.39R$, where ρ is the density in g cm^{-3} and R is the radius in Earth radii. For planets with radii > 1.5 $R_\oplus$, they apply a model of increasing H_2-He fraction with mass with a (nearly-linear) power law fit: $M = 2.69R^{0.93}$, where M and R are given in Earth masses and radii.

We fit these mass-radius fits to a data cube of our models with varying entropy, core mass, and envelope mass in Figures 8 and 9. In Figure 8 we employ models with Earth-like cores (32.5% Fe and 67.5% $MgSiO_3$), and in Figure 9, we employ models with pure water (Ice VII) cores. We plot each of our models as a point in (core mass)-(envelope mass) space. Each point corresponds to a particular total mass and a range of radii, depending on the envelope entropy. By setting the entropy to 5.5 (green), 6.0 (yellow), and 6.5 (red) k_B per baryon, we highlight those points that lie within 0.2 $M_\oplus$ of the mass-radius fit derived by Weiss & Marcy (2014). Following these highlighted points, we fit power laws in (core mass)-(envelope mass) space to the functional fit at each entropy. In general, we find a good fit to a power law, $M_{env} \propto M_c^x$, where $x = 8.0 - 8.5$ for rock-iron cores and

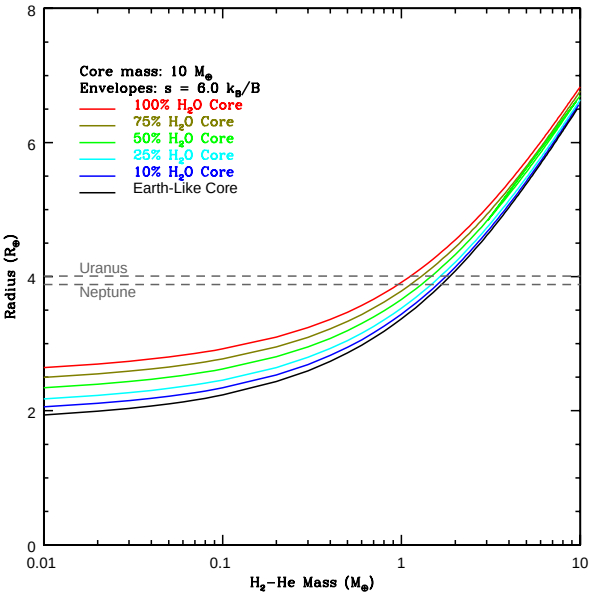

FIG. 6.— Radius versus envelope mass for planets with 10-$M_\oplus$ cores containing water layers (in the form of Ice VII) with mass fractions of 0%, 10%, 25%, 50%, 75%, and 100%. Envelope entropy is set to 6.0 k_B/B.

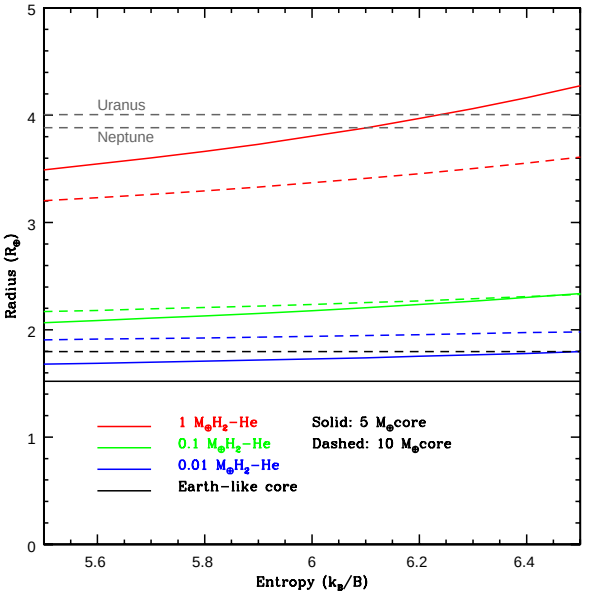

FIG. 7.— Radius versus entropy for planets with core masses of 5 and 10 $M_\oplus$. Curves with envelope masses of 0.01, 0.1, and 1.0 $M_\oplus$ are plotted. Entropy becomes a significant influence on the radius for large envelopes.

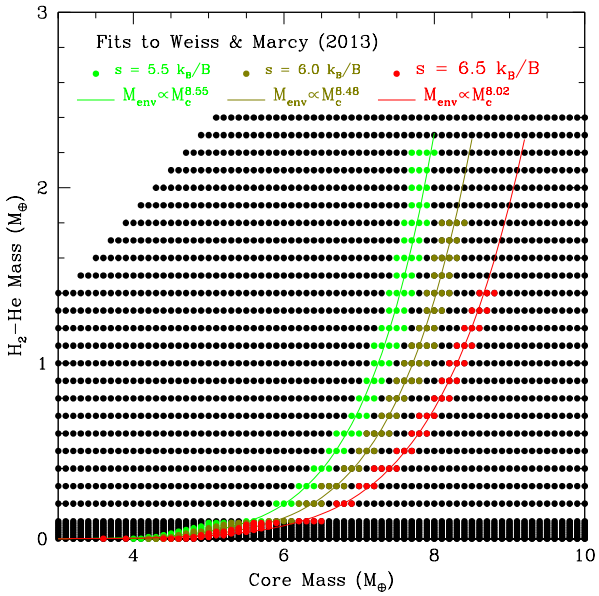

FIG. 8.— The functional mass-radius fit of Weiss & Marcy (2014) plotted through a data cube of our planet models (points) with varying entropy, core mass, and envelope mass, for Earth-like (iron-silicate) cores. Colored points lie within 0.2 $M_\oplus$ of this functional fit for an envelope entropy of 5.5 (green), 6.0 (yellow), and 6.5 (red) k_B/B. We fit a power law (shown) in (core mass)-(envelope mass) space to the functional fit for each entropy.

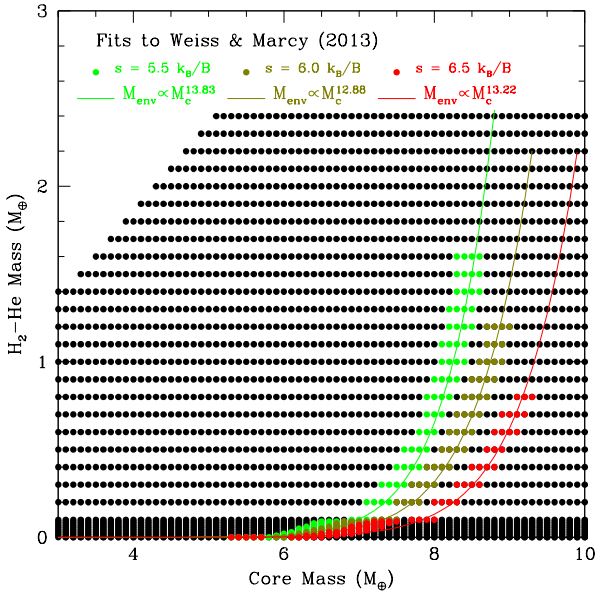

FIG. 9.— The functional mass-radius fit of Weiss & Marcy (2014) plotted through a data cube of our planet models (points) with varying entropy, core mass, and envelope mass, for pure water (Ice VII) cores. Colored points lie within 0.2 $M_\oplus$ of this functional fit for an envelope entropy of 5.5 (green), 6.0 (yellow), and 6.5 (red) k_B/B. We fit a power law (shown) in (core mass)-(envelope mass) space to the functional fit for each entropy.

$x = 13 - 14$ for pure ice cores, a very steep dependence of envelope mass on core mass.

However, Weiss & Marcy (2014) find an RMS deviation in mass around their fit of 4.3 $M_\oplus$, which can easily lead to a factor of two or more variation in total mass at a given radius. To address this, in Figures 10 and 11, we demonstrate the power of the core-envelope decomposition by plotting known planets on a grid of constant-core-mass and constant-envelope-mass curves (red) for two entropies of 5.5 and 6.5 k_B per baryon. In Figure 10, we employ models with Earth-like cores, and in Figure 11, we employ models with pure ice cores. With this grid, each mass-radius pair can be associated with a unique core mass and envelope mass for a given entropy and core type. The functional fit from Weiss & Marcy (2014) is also shown in blue in Figure 10.

Because of the larger radii of the ice cores, it takes significantly less envelope mass to produce the same radius for a given total mass. This allows us to extend Figure 11 to larger radii to reflect this, noting the detection of several more planets with large radii and envelope masses of $\sim 1 - 10$ $M_\oplus$ in this case.

We provide the quantitative core-envelope decomposition for observed exoplanets and Solar System planets in Table 2 in both the rocky-iron core and ice core cases for an envelope entropy of 6.0 k_B per baryon. If the observed radius is smaller than a bare core of the observed mass for one or both core types, we still include the decomposition with an envelope mass of zero.

The core-envelope decompositions readily reveal useful information about the structures of planets from mass-radius data. For example, the low-density planet Kepler-11e (the topmost point plotted in Figure 10), can be fit to a model with a large H_2-He fraction based on an Earth-like core mass of 6.3 $M_\oplus$ and an envelope mass of 2.1 $M_\oplus$, for an entropy for 6.0 k_B per baryon, with small differences for a different entropy[7], or an icy core mass of 6.8 $M_\oplus$ and envelope mass of 1.6 $M_\oplus$. In contrast, the higher-density planet Kepler-131b (the bottom-rightmost point) can be fit to a model with a small H_2-He fraction based on an Earth-like core mass of 15.98 $M_\oplus$ and an envelope mass of 0.15 $M_\oplus$ at an entropy of 6.0 k_B per baryon. For an ice core, the bare core would suffice.

The difference in envelope mass between an Earth-like core model and an ice core model can be as small as 0.059 $M_\oplus$ while still retaining some envelope (e.g. Kepler-98b), but is usually a few tenths of an Earth mass. The largest difference of 1.1 $M_\oplus$ occurs for Neptune.

We note a small number of planets with masses of $2-20$ $M_\oplus$ and very large radii (for these masses) of $5-7$ $R_\oplus$, as shown in Figure 11. While additional planet detections and further investigation with gas giant models is needed to investigate these objects in detail, we see from these objects that large envelope fractions can occur even for low-mass planets. In the most extreme case we study, Kepler-79d (the topmost point in Figure 11), we find a core mass of 2.0 $M_\oplus$ and an envelope mass of 4.0 $M_\oplus$ for the case of a pure ice core and entropy of 6.0 k_B per baryon, equivalent to an envelope mass fraction of 67%.

[7] Increasing the entropy of the models shifts the grid up and to the left, making it straighter, and fits a higher core mass and lower envelope mass to the same mass and radius.

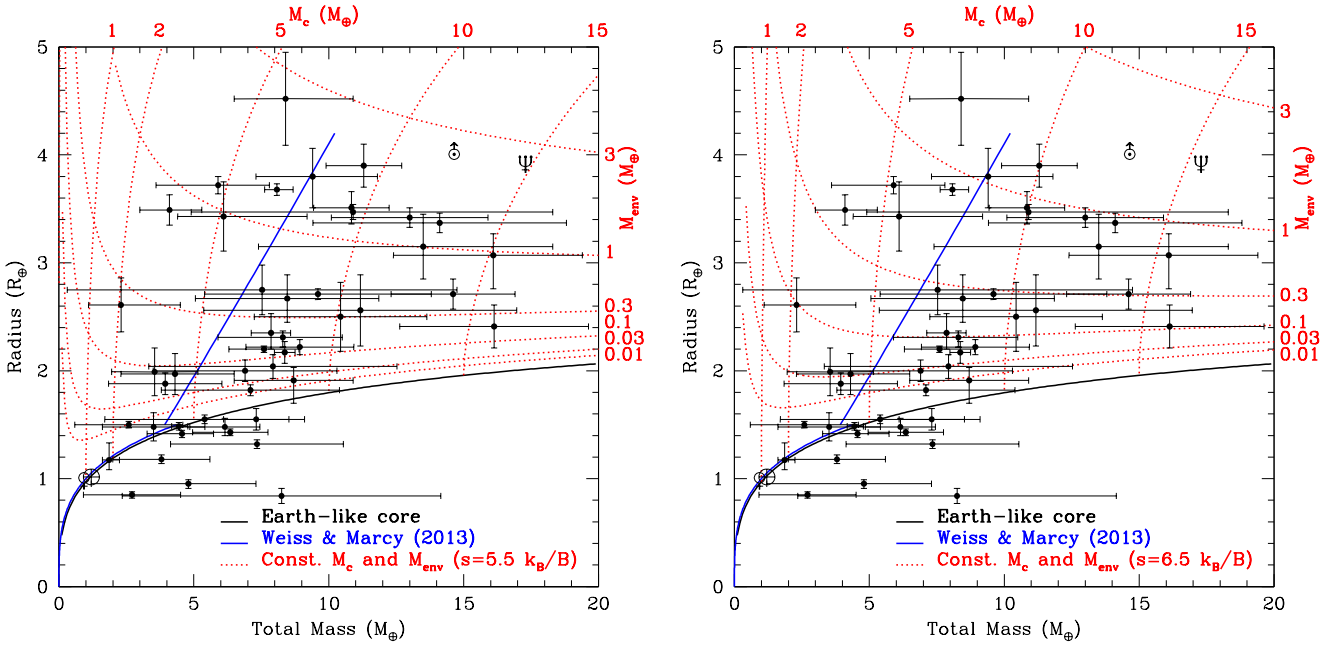

FIG. 10.— Known extrasolar planets plotted against the observational mass-radius fits of Weiss & Marcy (2014) (blue) and a grid of constant core mass and envelope mass curves (red) for planets with Earth-like (iron-silicate) cores. Curves with entropies of 5.5 and 6.5 k_B/B are plotted.

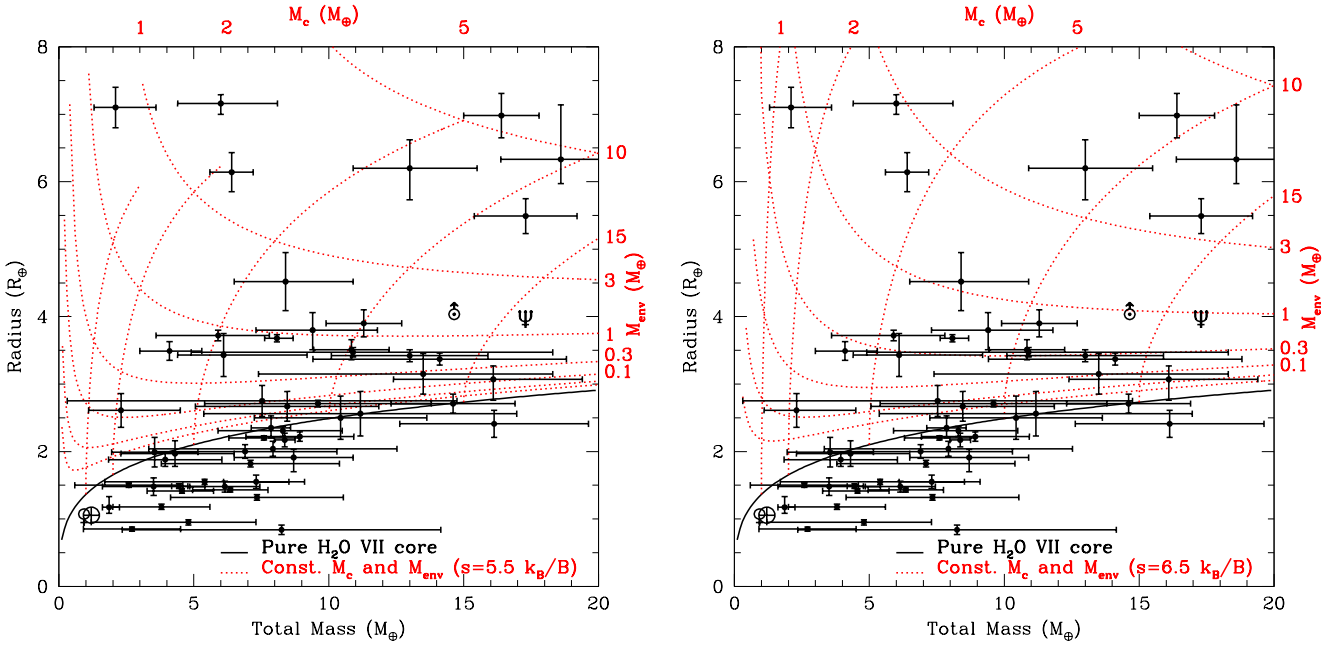

FIG. 11.— Known extrasolar planets plotted against the observational mass-radius fits of Weiss & Marcy (2014) (blue) and a grid of constant core mass and envelope mass curves (red) for planets with pure water (Ice VII) cores. Curves with entropies of 5.5 and 6.5 k_B/B are plotted.

TABLE 2
Masses and Radii of Observed Exoplanets and Theoretical Decomposition into Core and Envelope Components ($s = 6.0k_B/B$)

Planet	Radius ($R_\oplus$)	Mass ($M_\oplus$)	M_c ($M_\oplus$) (Fe/Rock Core)	M_{env} ($M_\oplus$) (Fe/Rock Core)	M_c ($M_\oplus$) (H_2O Core)	M_{env} ($M_\oplus$) (H_2O Core)	References
55 Cancri e	2.17 ± 0.10	8.37 ± 0.38	8.284	0.086	8.37	0.00	1,2
CoRoT-7b	1.55 ± 0.10	7.31 ± 1.21	7.31	0.00	7.31	0.00	3
GJ 1214b	2.65 ± 0.09	6.45 ± 0.91	6.15	0.30	6.396	0.054	4
GJ 3470b	4.20 ± 0.60	14.0 ± 1.8	11.6	2.4	12.5	1.5	5
HAT-P-26b	$6.33^{+0.81}_{-0.36}$	18.60 ± 2.22	9.9	8.7	10.9	7.7	6
HD 97658b	$2.35^{+0.18}_{-0.15}$	7.86 ± 0.73	7.50	0.36	7.86	0.00	7
Kepler-10b	$1.416^{+0.033}_{-0.036}$	$4.56^{+1.17}_{-1.29}$	4.56	0.00	4.56	0.00	8
Kepler-11b	1.97 ± 0.19	$4.3^{+2.2}_{-2.0}$	4.247	0.053	4.3	0.00	9
Kepler-11c	3.15 ± 0.30	$13.5^{+4.8}_{-6.1}$	12.66	0.84	13.32	0.18	9
Kepler-11d	3.43 ± 0.32	$6.1^{+3.1}_{-1.7}$	5.35	0.75	5.67	0.43	9
Kepler-11e	4.52 ± 0.43	$8.4^{+2.5}_{-1.9}$	6.3	2.1	6.8	1.6	9
Kepler-11f	2.61 ± 0.25	$2.3^{+2.2}_{-1.2}$	2.14	0.16	2.226	0.074	9
Kepler-18b	2.00 ± 0.10	6.9 ± 3.4	6.856	0.044	6.9	0.00	10
Kepler-18c	5.49 ± 0.26	17.3 ± 1.9	11.5	5.8	12.5	4.8	10
Kepler-18d	6.98 ± 0.33	16.4 ± 1.4			7.3	9.1	10
Kepler-20b	$1.91^{+0.12}_{-0.21}$	8.7 ± 2.2	8.688	0.012	8.7	0.00	11
Kepler-20c	$3.07^{+0.20}_{-0.31}$	$16.1^{+3.3}_{-3.7}$	15.30	0.80	16.02	0.098	11
Kepler-20d	2.75 ± 0.23	7.53 ± 7.22	7.16	0.37	7.461	0.069	12
Kepler-25b	2.71 ± 0.05	9.6 ± 4.2	9.23	0.37	9.572	0.028	12
Kepler-30b	3.90 ± 0.20	11.3 ± 1.4	9.6	1.7	10.31	0.99	13
Kepler-36b	1.486 ± 0.035	$4.45^{+0.33}_{-0.27}$	4.45	0.00	4.45	0.00	14
Kepler-36c	3.679 ± 0.054	$8.08^{+0.60}_{-0.46}$	6.96	1.12	7.41	0.67	14
Kepler-48b	1.88 ± 0.10	3.94 ± 2.10	3.902	0.038	3.94	0.00	12
Kepler-48c	2.71 ± 0.14	14.61 ± 2.30	14.21	0.40	14.61	0.00	12
Kepler-48d	2.04 ± 0.11	7.93 ± 4.60	7.883	0.047	7.93	0.00	12
Kepler-50b	2.20 ± 0.03	7.6 ± 1.3	7.5	0.10	7.6	0.00	15
Kepler-51b	7.10 ± 0.30	$2.1^{+1.50}_{-0.80}$			0.84	1.26	16
Kepler-57c	1.55 ± 0.04	5.4 ± 3.7	5.4	0.00	5.4	0.00	15
Kepler-68b	$2.31^{+0.06}_{-0.09}$	$8.3^{+2.2}_{-2.4}$	8.16	0.14	8.3	0.00	17
Kepler-68c	$0.953^{+0.037}_{-0.042}$	$4.8^{+2.5}_{-3.6}$	4.8	0.00	4.8	0.00	17
Kepler-78b	$1.173^{+0.159}_{-0.089}$	$1.86^{0.38}_{-0.25}$	1.86	0.00	1.86	0.00	18
Kepler-79b	3.47 ± 0.07	$10.9^{7.4}_{-6.0}$	9.79	1.11	10.4	0.50	19
Kepler-79c	3.72 ± 0.08	$5.9^{1.9}_{-2.3}$	4.97	0.93	5.28	0.62	19
Kepler-79d	$7.16^{+0.13}_{-0.16}$	$6.0^{2.1}_{-1.6}$			2.0	4.0	19
Kepler-79e	3.49 ± 0.14	$4.1^{1.2}_{-1.1}$	3.51	0.59	3.71	0.39	19
Kepler-87c	6.14 ± 0.29	6.4 ± 0.8			3.3	3.1	20
Kepler-89c	$3.80^{+0.26}_{-0.29}$	$9.4^{-2.4}_{-2.1}$	8.0	1.4	8.58	0.82	21
Kepler-89e	$6.20^{+0.42}_{-0.47}$	$13.0^{-2.5}_{-2.1}$			7.3	5.7	21
Kepler-93b	1.50 ± 0.03	2.59 ± 2.00	2.585	0.005	2.59	0.00	12
Kepler-94b	3.51 ± 0.15	10.84 ± 1.40	9.69	1.15	10.30	0.54	12
Kepler-95b	3.42 ± 0.09	13.0 ± 2.9	11.85	1.15	12.57	0.43	12
Kepler-96b	2.67 ± 2.22	8.46 ± 3.40	8.12	0.34	8.428	0.032	12
Kepler-97b	1.48 ± 0.13	3.51 ± 1.90	3.509	0.001	3.51	0.00	12
Kepler-98b	1.99 ± 0.22	3.55 ± 1.60	3.491	0.059	3.5496	0.0004	12
Kepler-99b	1.48 ± 0.08	6.15 ± 1.30	6.15	0.00	6.15	0.00	12
Kepler-100b	1.32 ± 0.04	7.34 ± 3.20	7.34	0.00	7.34	0.00	12
Kepler-102b	1.18 ± 0.04	3.8 ± 1.8	3.8	0.00	3.8	0.00	12
Kepler-102e	2.22 ± 0.07	8.93 ± 2.00	8.83	0.010	8.93	0.00	12
Kepler-103b	3.37 ± 0.09	14.11 ± 4.70	12.97	1.14	13.75	0.36	12
Kepler-106c	2.50 ± 0.32	10.44 ± 3.20	10.20	0.24	10.44	0.00	12
Kepler-106e	2.56 ± 0.33	11.17 ± 5.80	10.89	0.28	11.17	0.00	12
Kepler-113b	1.82 ± 0.05	7.1 ± 3.3	7.091	0.009	7.1	0.00	12
Kepler-131b	2.41 ± 0.20	16.13 ± 3.50	15.98	0.15	16.13	0.00	12
Kepler-131c	0.84 ± 0.07	8.25 ± 5.90	8.25	0.00	8.25	0.00	12
Kepler-406b	1.43 ± 0.03	6.35 ± 1.40	6.35	0.00	6.35	0.00	12
Kepler-406c	0.85 ± 0.03	2.71 ± 0.80	2.71	0.00	2.71	0.00	12
Uranus	4.007	14.536	12.3	2.1	14.5	1.2	
Neptune	3.883	17.147	16.0	2.1	16.1	1.0	

References. — (1) Gillon et al. (2012) (2) Endl et al. (2012); (3) Moutou et al. (2013); (4) Carter et al. (2011); (5) Crossfield et al. (2013); (6) Hartman et al. (2011); (7) Dragomir et al. (2013); (8) Batalha et al. (2011); (9) Lissauer et al. (2011); (10) Cochran et al. (2011); (11) Gautier et al. (2012); (12) Weiss & Marcy (2014); (13) Sanchis-Ojeda et al. (2012); (14) Carter et al. (2012); (15) Steffen et al. (2013); (16) Masuda (2014b); (17) Gilliland et al. (2013); (18) Pepe et al. (2013); (19) Jontof-Hutter et al. (2013); (20) Ofir et al. (2014); (21) Masuda et al. (2013);

Similar results occur for a wide range of masses. We find Kepler-51b, with a total mass of 2.1 $M_\oplus$, to have an envelope mass fraction of 60%, and Kepler-18d, with a total mass of 16.4 $M_\oplus$, to have an envelope mass fraction of 55%, both in the case of a pure ice core.

This core-envelope decomposition for observed planets, especially when the large-radius planets are included, implies that envelope mass can vary from zero to greater than the core mass for the entire range of masses we study, except that we find a lower limit of envelope mass of $\sim$0.1 $M_\oplus$ in the case of Earth-like cores with masses of $\sim 8-20$ $M_\oplus$. While we do see the trend of decreasing density for masses > 7.6 $M_\oplus$ observed by Weiss & Marcy (2014), with a broad scatter of the observed planets centered around the functional fit, the spread in core mass and envelope mass is so wide that we see only a slight justification for any given functional fit.

We consider the possibility of multiple populations of planets in envelope mass space—one with $M_{env} \gtrsim 3$ $M_\oplus$, one with $M_{env} \sim 1$ $M_\oplus$, and one with $M_{env} \lesssim 0.3$ $M_\oplus$, but the statistics are not sufficient to tell whether these populations are distinct. In any case, it is clear that a significant amount of H_2-He ($\sim$1 $M_\oplus$) is needed to produce the large radii observed for many low-mass planets. We also note that many of the newly-discovered planets fall in the 5–10 $M_\oplus$ core mass range, but, again, it is not clear if this genuinely reflects the true underlying distribution function, or is due to statistics and selection biases.

5. INTERNAL STRUCTURES

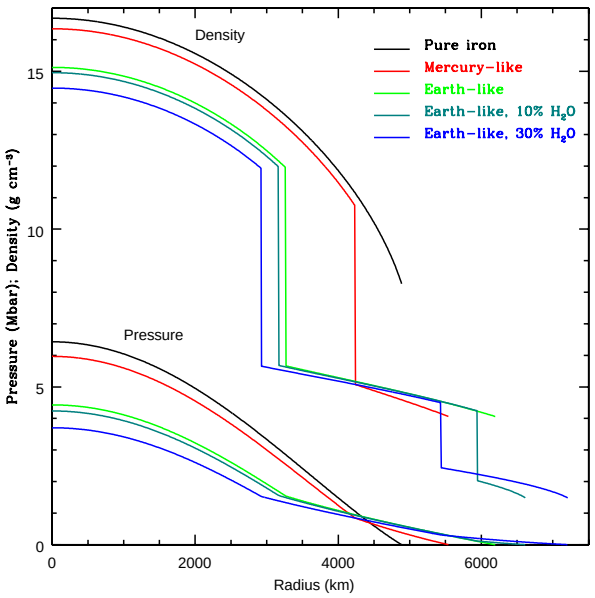

FIG. 12.— Density and pressure profiles of various iron core/$MgSiO_3$ mantle planets, including two with deep water layers, all 1 $M_\oplus$. "Earth-like" is defined as a 13:27 ratio of iron to $MgSiO_3$ mass, and "Mercury-like" is defined as 7:3 ratio of iron to $MgSiO_3$ mass, corresponding to the compositions of Earth and Mercury when water is not included. Planets with a greater core mass fraction have a smaller radius for a given mass due to the high density of iron relative to that of $MgSiO_3$.

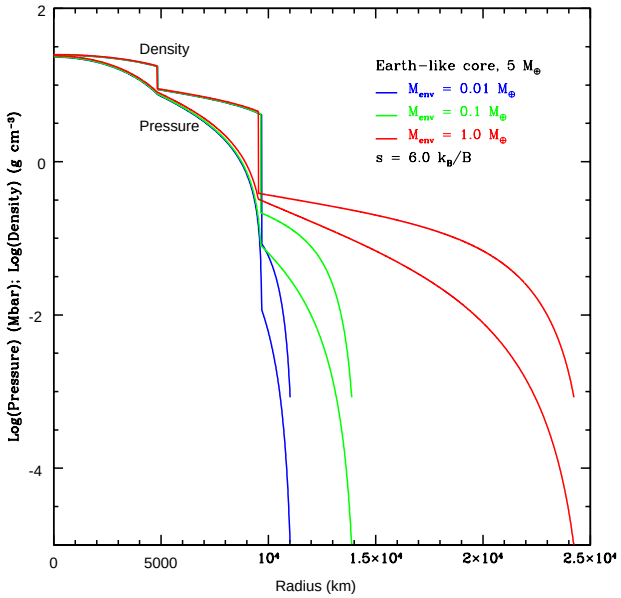

FIG. 13.— Density and pressure profiles of planets with a 5-$M_\oplus$ Earth-like core plus H_2-He envelopes equal to 0.01, 0.1, and 1.0 $M_\oplus$. In each case, the envelope has a constant entropy of 6.0 k_B/B. Increasing the envelope mass compresses the core slightly, making the core radius smaller.

In this section, we provide several figures relating to the internal structures of the planets we model. Figure 12 shows pressure and density profiles of several representative solid planet models, each with a mass of 1 $M_\oplus$. We include pure iron, Mercury-like, and Earth-like compositions, along with "water-worlds" that are otherwise Earth-like, but have 10% and 30% water (Ice VII). Similarly, Figure 13 shows pressure and density profiles of representative models with H_2-He envelopes. These models each have a core mass of 5 $M_\oplus$ and entropy of 6.0 k_B per baryon, and envelope masses of 0.01, 0.1, and 1.0 $M_\oplus$ are plotted. Increasing the envelope mass slightly compresses the core, decreasing the core radius.

Figure 14 shows the base pressure of the envelope versus envelope mass *fraction* (f_{env}) for models with various constant core masses. For shallow envelopes for which the gravity does not vary significantly, the expected base pressure is

$$P_b \approx \frac{M_{env} g}{4\pi R^2} \approx \frac{G M_c M_{env}}{4\pi R^4} \approx \frac{G M_c^2 f_{env}}{4\pi R^4}, \qquad (2)$$

where g is the surface gravity. This relation holds well for small envelope mass fractions, but the pressure is lower than the relation would imply for envelope mass fractions $\gtrsim 3\%$ due to the variation in gravity over the height of the envelope.

For low envelope fractions, the plot also shows a relation remarkably close to $P_b \propto M_c$. Figure 15 shows why this is so, plotting envelope base pressure versus *core* mass for constant envelope masses of 0.01, 0.1, and 1.0 $M_\oplus$. The envelope base pressure in nearly constant over a wide range of core masses for shallow envelopes. Evidently, based on the relation above, M_c/R^4 is nearly constant for these models. This is supported by our power law fit for Earth-like solid planets of $R \propto M^{0.266-0.274}$

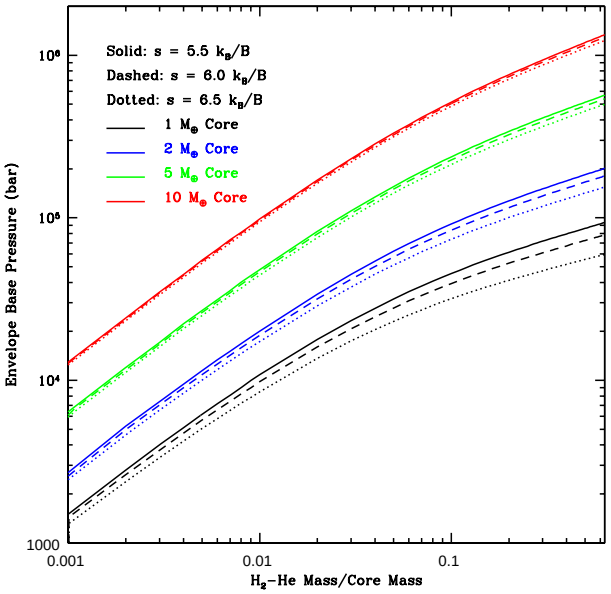

FIG. 14.— Pressure at the base of the envelope versus envelope mass fraction for planets with constant core masses of 1, 2, 5, and 10 $M_\oplus$. Curves with entropies of 5.5, 6.0, and 6.5 k_B/B are plotted.

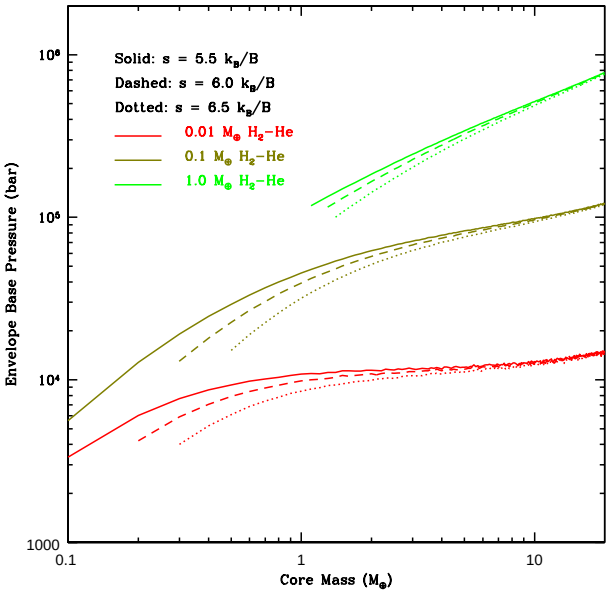

FIG. 15.— Pressure at the base of the envelope versus core mass for planets with constant envelope masses of 0.01, 0.1, and 1.0 $M_\oplus$. Curves with entropies of 5.5, 6.0, and 6.5 k_B/B are plotted.

(see Section 6). On the other hand, if the core mass is low enough that the H_2-He comprises $\gtrsim$10% of the total mass, then the base pressure increases roughly linearly with core mass. Also, the entropy begins to have a significant effect on the base pressure in models with small cores, likely due to the increasing dependence of the radius on entropy as the core mass decreases (see Figure 4).

We also plot curves of central pressure and density versus envelope mass for models with a constant core mass

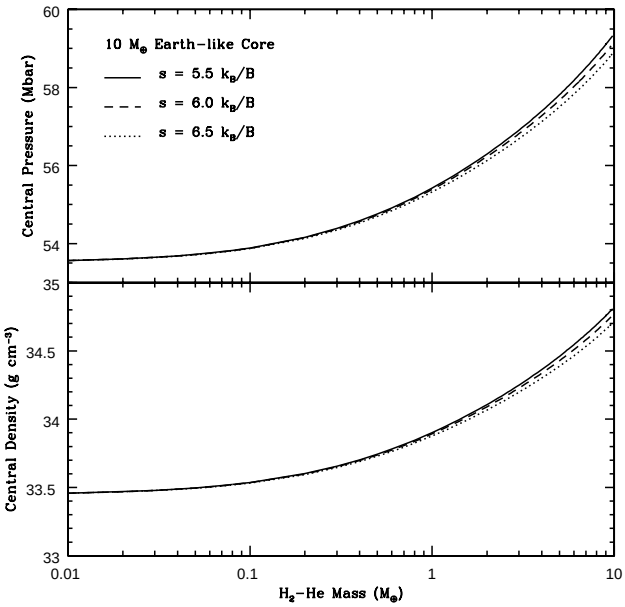

FIG. 16.— Central pressure (top) and density (bottom) of planets with a 10-$M_\oplus$ Earth-like core and a variable envelope mass. Entropies of 5.5, 6.0, and 6.5 k_B/B are plotted. Despite a large change in total mass, the central pressure and density change very little.

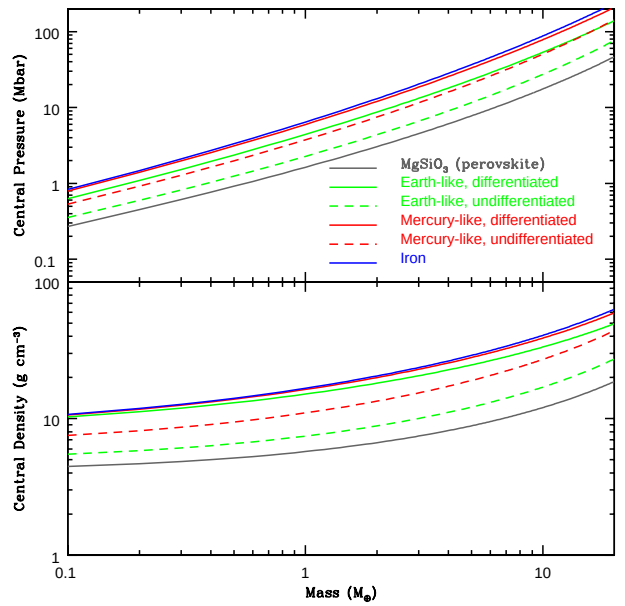

FIG. 17.— Central pressure (top) and density (bottom) as a function of mass for constant-composition iron core/$MgSiO_3$ (perovskite) mantle planets in the 0.1−20 $M_\oplus$ range. The iron mass fractions shown are 0%, 32.5% (Earth-like), 70% (Mercury-like) and 100%. Solid lines are differentiated, dashed lines are undifferentiated.

of 10 $M_\oplus$ and entropies of 5.5, 6.0, and 6.5 k_B per baryon. Despite a large change in total mass, the central pressure and density change very little—about 5% in density and 10% in pressure for a doubling of total mass.

Central pressure and density versus (total) mass curves for representative solid planets, both differentiated and

undifferentiated, are compared in Figure 17. The pure $MgSiO_3$ (perovskite) planet profile is included in order to demonstrate the discontinuity that arises in central density when a material of higher density is added. The planets with iron cores all have very similar central densities, while undifferentiated planets with varying iron fractions have lower central densities. This pattern repeats to a lesser degree for central pressures.

6. SOLID EXOPLANETS

For completeness, we now provide mass-radius curves and tables for a range of solid exoplanet models with no significant envelopes. We construct true "terrestrial" planets with iron and $MgSiO_3$ components as well as three-component models with iron, $MgSiO_3$, and water, in the form of Ice VII, corresponding to "water worlds." Figure 1 shows mass-radius plots for some of our representative solid planet models compared with masses and radii of observed exoplanets.

While we compute each curve from 0.1 to 20 $M_\oplus$, our core-envelope decomposition results suggest that planets larger than $\sim$8 $M_\oplus$ will likely have gaseous envelopes. Therefore our models of solid planets likely should only be applied to planets $\lesssim$8 $M_\oplus$ that do not have extended envelopes. However, gaseous envelopes of close-orbiting planets could later be stripped away by evaporation by XUV irradiation, particularly for planets with initial masses $\lesssim$0.3 M_J orbiting young Solar-type stars (Hubbard et al. 2007).

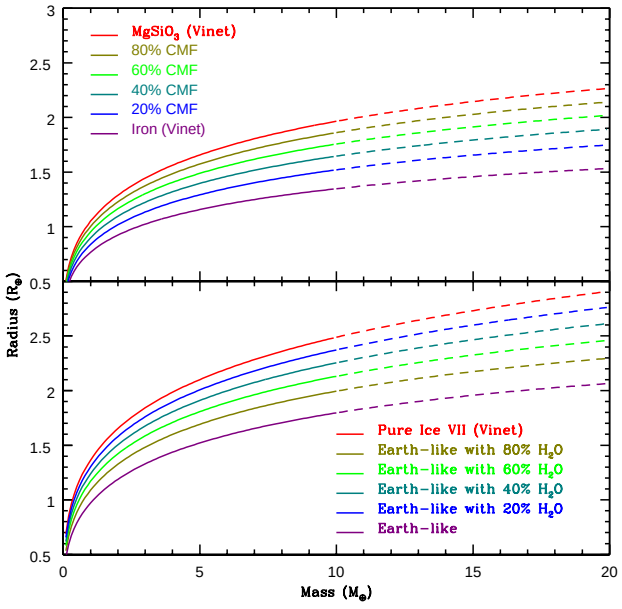

FIG. 18.— Mass-radius curves for solid planets with various core mass fractions (CMF) ranging from 0% to 100%. Top panel: terrestrial models with iron cores and $MgSiO_3$ mantles. Bottom panel: "water worlds" with "cores" having an Earth-like structure plus a deep water layer (in the form of Ice VII).

In Figure 18, we plot terrestrial models with different iron core mass fractions (CMFs), ranging from pure iron to pure $MgSiO_3$ (perovskite), showing a systematic trend of decreasing radius with increasing CMF. We also plot models of "water worlds" with an Earth-like core (Earth-like in having the same Fe/Mg ratio as Earth), ranging from a purely Earth-like composition to pure water. Because the water worlds have some iron content, they overlap with terrestrial models with lower iron content, even given the lower density of water, pointing to a degeneracy with composition in the mass-radius plot.

A power-law fit of the form $R \propto M^x$ provides a simple description of the behavior of the mass radius curves. Valencia et al. (2006) performed such a fit over the span of their "super-Earths" (1−10 Earth masses, 33% CMF) and "super-Mercurys" (1−10 Mercury masses, 70% CMF), and we compute the values of x in our fits for comparison. For "super-Earths," we find a power-law coefficient of 0.266−0.274, while Valencia et al. (2006) reported a range of 0.267−0.272. For "super-Mercurys,", we find a power-law coefficient of 0.309−0.312, comparable to the "$\sim$0.3" reported by Valencia et al. (2006). The lower masses of the "super-Mercurys" result in less compression in their interiors, and a power-law fit closer to the $R \propto M^{\frac{1}{3}}$ law for uncompressed planets than for super-Earths.

The super-Earths with currently observed masses and radii consistent with a purely solid composition have masses of $\sim 2-8$ $M_\oplus$. While these numbers are loose, we can use them in conjunction with our models to study the relation between radius and composition. For example, in this $\sim 2-8$ $M_\oplus$ range, the range of radii for pure iron models (the minimum radius for a given mass) is $\sim 0.9-1.3$ $R_\oplus$, in contrast with the range for pure silicates (the maximum radius for terrestrial compositions), which have radii of $\sim 1.25-2.0$ $R_\oplus$, and water-rich models, which are larger still. While there are significant degeneracies with composition among solid planets, this reiterates the usefulness of radius as a proxy for distinguishing solid exoplanets from those with gaseous envelopes, since planets larger than 2 $R_\oplus$ cannot be purely rock/iron and are likely to have such gaseous envelopes (Lopez & Fortney 2013; Weiss & Marcy 2014; Marcy et al. 2014a).[8]

Properties of differentiated planet models with Earth-like and Mercury-like compositions are given in Tables 12 and 14, respectively. For comparison, we present properties of pure iron and pure silicate planets in Tables 11 and 16, respectively.

7. CONCLUSIONS

We have investigated a range of exoplanet models for various core masses, gaseous envelope masses, and envelope entropies, and compared them with mass and radius observations. Some of our representative modeled planet properties are tabulated in Tables 5-16 for a variety of planet compositions. We have explored models with both "Earth-like" rock-iron cores and ice cores to account for the possibility of the formation of planets with gaseous envelopes in both the warm and cold regions of their "solar" systems. We also considered varying silicate and water fractions for solid planets.

We have decomposed observed exoplanets into core mass and envelope mass components for both rock-iron cores and ice cores. Based on measured masses and radii,

[8] However, further work may be needed to distinguish planets with an H_2-He envelope from the potential population of water-rich planets.

we find that the envelope mass, M_{env}, may vary over a wide range of values from zero to greater than the mass of the core itself over a wide range of total masses, except that for the higher-mass "sub-Neptune" (or "mini-Neptune") planets, a nonzero envelope mass is always required to fit a rock-iron core. Thus, planetary formation and evaporation models need to account for the very wide range of core masses and envelope masses derived.

In general, an ice core model requires a smaller envelope mass (and larger core mass) to fit the same mass-radius pair as an Earth-like core model, because of the larger radius of the core. Entropy also has a systematic effect on the core-envelope decomposition: an envelope with higher entropy is hotter and has a lower density, so that a smaller envelope mass is needed to fit the same mass-radius pair. Therefore, given these uncertainties, we have derived a range of possible core and envelope masses for known Neptune- and sub-Neptune-sized exoplanets.

While a few planets have large envelope mass fractions of $\sim 44\%-67\%$, as shown in Figure 11 and Table 2, most of the "sub-Neptune" planets that have been observed are dominated by their core masses (Figures 10 and 11); that is, the envelope comprises only a small fraction of the total mass. At the same time, for core masses of $M_c \gtrsim 5$ $M_\oplus$, the planetary radius is very sensitive to the envelope mass and also to the entropy, so that the observed radius can serve as a proxy for the properties of the envelope, subject to the degeneracies of envelope mass and entropy.

For solid planets, we find that only planets with radii $\lesssim 1.5-2.0$ $R_\oplus$ can be purely terrestrial (iron core plus silicate mantle). Observationally, the largest planet that is consistent with our terrestrial models is Kepler-20b, with $M = 8.7 \pm 2.2$ $M_\oplus$ and $R = 1.91^{+0.12}_{-0.21}$ $R_\oplus$. In a transitional regime of $\sim$1.75-2.8 $R_\oplus$ (which may correspond with an observed break in the planetary occurence function, Batalha et al. 2013), the abundance of both water and H_2-He may be important, but the effect of the water fraction on the radius diminishes for larger planets.

Determining the composition and structure of solid planets from mass and radius observations is more ambiguous than for planets with gaseous envelopes due to significant degeneracies and uncertainties. There is overlap in radius with different iron fractions and water fractions over the mass range at which planets with potentially-solid compositions have been observed. Further research is needed to standardize equations of state for planetary models (Nettelmann et al. 2008) and reduce uncertainties.

There remains a degeneracy between composition and envelope entropy, and more detailed atmospheric and evolutionary models are needed to precisely estimate the atmospheric entropy of exoplanets (to a precision of $\sim 0.1 k_B/B$) in order to make more accurate determinations of their compositions and envelope/core mass partitions. On the observational side, more precise mass measurements are needed to better constrain core masses, as well as envelope masses in the case of smaller planets. More planet detections with overall better statistics are also needed to fully populate the mass-radius diagram and determine the distinct populations of planets (if any) in this regime.

A.B. would like to acknowledge support in part under NASA ATP grant NNX07AG80G, HST grants HST-GO-12181.04-A, HST-GO-12314.03-A, HST-GO-12473.06-A, and HST-GO-12550.02, and JPL/Spitzer Agreements 1417122, 1348668, 1371432, 1377197, and 1439064.

APPENDIX

RADIUS CODE VERIFICATION

Our computational procedure for deriving planet structural profiles and the corresponding mass-radius relationships is as follows: We begin with a guess of central pressure and integrate the equations of hydrostatic equilibrium out until the pressure is zero. For differentiated planets, we dictate a boundary mass for the core material, at which we switch to the equation of state for the new material, maintaining pressure continuity. Our code admits an arbitrary number of layers of different materials. Because it is impossible to know the total mass or radius before the integration is performed, we use an iterative Newton-Raphson scheme to produce a planet of specified mass.

For hydrogen-helium envelopes, we assume an adiabatic pressure and density profile by setting a constant entropy, usually at $5.5-6.5$ k_B per baryon. This is approximately correct for a convective envelope, except near the surface, where the atmosphere becomes radiative, with the caveat that highly irradiated planets may be radiative to significant depths. The code also relies on extrapolations for pressures of less than 10 bars. (Pressures this low are not encountered in solid planets.)

We use a fourth-order Runge-Kutta scheme to solve the equations of hydrodynamic equilibrium:

$$\frac{dP}{dr} = -\frac{Gm\rho}{r^2} \tag{A1}$$

$$\frac{dm}{dr} = 4\pi r^2 \rho, \tag{A2}$$

where r is the radius, ρ is the mass density, $P(\rho)$ is the pressure given by the EOS, and m is the mass interior to r. We use various radius step sizes ranging from 10−100m depending on the size of the planet model.

We test our code with the polytropic equation of state, $P = K\rho^{1+\frac{1}{n}}$ with n =1.5, 2, 2.5, and 3. Our results for the constants $\rho_c/\bar{\rho}$ (scaled density) and ξ (scaled radius) agree with the values found in Chandrasekhar (1939) to a part in 10^5.

EQUATIONS OF STATE

For solid planets, we implement two semi-empirical equations of state for most materials. The first is the third-order Birch-Murnagham EOS, given by

$$P_3 = \frac{3}{2}K_0\left[x^{\frac{7}{3}} - x^{\frac{5}{3}}\right]\left\{1 + \frac{3}{4}\left(K_0' - 4\right)\left[x^{\frac{2}{3}} - 1\right]\right\}, \tag{B1}$$

where x is the ratio ρ/ρ_0, ρ_0 is the zero-pressure density, K_0 is the bulk modulus at $\rho = \rho_0$, and K_0' is the pressure derivative of the bulk modulus at $\rho = \rho_0$. Values for the second pressure derivative of the bulk modulus at $\rho = \rho_0$, K_0'', are in most cases not available, but for materials which have a known K_0'', a fourth-order term can be added to the third-order B-M EOS:

$$\begin{aligned} P_4 =& P_3 + \frac{3}{2}K_0\left[x^{\frac{7}{3}} - x^{\frac{5}{3}}\right]\frac{3}{8}\left(x^{\frac{2}{3}} - 1\right)^2 \\ &\times\left[K_0K_0'' + K_0'\left(K_0' - 7\right) + \frac{143}{9}\right]. \end{aligned} \tag{B2}$$

The second semi-empirical equation of state that we implement is the Vinet EOS, given by

$$P = 3K_0x^{2/3}\left[1 - x^{-\frac{1}{3}}\right]\exp\left(\frac{3}{2}\left(K_0' - 1\right)\left[1 - x^{-\frac{1}{3}}\right]\right). \tag{B3}$$

A summary of the equations of state used in our models is given in Table 3.

TABLE 3
EQUATIONS OF STATE USED FOR THIS PROJECT[a]

Material	EOS	ρ_0 (g cm^{-3})	K_0 (Mbar)	K_0'	Ref
Fe (ϵ)	Vinet	8.267	1.634	5.38	1
$MgSiO_3$ (perovskite)	Vinet	4.064	2.48	3.91	2
MgO (periclase)	B-M3	3.5833	1.602	3.99	3
SiC (ZB)[b]	B-M3	3.350	2.271	3.79	4
SiC (RS)[b]	B-M3	4.256	2.666	4.64	4
Diamond	Vinet	3.5171	4.45	4.0	5
Platinum	Vinet	21.46	2.70	5.64	6
H_2O Ice VII	Vinet	1.4876	1.49	6.2	7
H_2-He	Tabular				8

[a] All of the values are for materials at zero pressure and temperature. ρ_0 is the density, K_0 is the bulk modulus, and K_0' is the pressure derivative of the bulk modulus.
[b] The SiC EOS with zincblende (ZB) structure is used for pressures up to 0.75 Mbar, beyond which the EOS with rock salt (RS) structure is used.

REFERENCES. — (1) Dewaele et al. (2006); (2) Tsuchiya et al. (2004); (3) Speziale et al. (2001); (4) Lu et al. (2008); (5) Kunc et al. (2003); (6) Sun et al. (2008); (7) Wolanin et al. (1997); (8) Saumon et al. (1995);

Which EOS fit is used for a given material makes little difference at low pressures where the zero-pressure density dominates. In Figure 19, models using the Vinet and B-M semi-empirical equations of state for pure $MgSiO_3$ (perovskite) are used to generate mass-radius curves, which differ by only 0.3% for 1 Earth-mass planets, 0.3% for 5 Earth-mass planets, and 1.2% for 10 Earth-mass planets. These results agree with those reported in Seager et al. (2007), who found that the mass-radius curves for low-mass exoplanets depend only on the uncompressed density. The differences become more significant for planets of higher mass (and, therefore, higher internal pressure), amounting to ∼3.3% for 20 Earth-mass silicate planets and 7.0% for 20 Earth-mass iron planets, although we do not expect to see solid planets of this size without H_2-He envelopes (Lopez & Fortney 2013; Weiss & Marcy 2014). A more detailed summary of differences is given in Table 4.

TABLE 4
DIFFERENCE IN RADIUS BETWEEN PLANETS WITH VINET AND B-M EQUATIONS OF STATE

Mass ($M_\oplus$)	Pure Fe	Pure $MgSiO_3$	Pure H_2O
1.0	0.072%	-0.286%	0.239%
5.0	1.64%	0.251%	0.417%
10.0	3.58%	1.17%	1.06%
20.0	7.02%	3.27%	2.38%

To better illustrate the differences between the various equations of state, the pressure-density curves for various EOSs fits for Mg_2SiO_4 (olivine) and $MgSiO_3$ (perovskite) are plotted in Figure 20 over the run of pressures found in super-Earths of mass up to 20 Earth masses (without gaseous envelopes). The curves show significant divergence in pressure at high densities, particularly for the different Mg_2SiO_4 EOSs, but remarkable similarities between the two materials, demonstrating that for rocky material, the choice of equation of state is more important than the precise chemical composition. For this reason, we do not address phase transitions in the mantle. This similarity breaks down below ∼1 Mbar, however, where the uncompressed density dominates. Notably, the < 1 Mbar range includes most of the mantle of a 1-$M_\oplus$ Earth-like planet, so the choice of phase transitions and the choice of silicate material could have a significant effect for lower-mass planets.

For context, internal pressure and density profiles for model 1-$M_\oplus$ planets of various compositions are plotted in Figure 12. Poirier (2000) and Hama & Suito (1996) report that the Vinet EOS is more suited to extrapolation to high pressures. However, as Table 1 demonstrates, a wide variety of EOS data and fits have been used in the literature. Unless otherwise specified, we use a Vinet EOS in building our models, but we also use a 3rd-Order B-M EOS in some cases, as indicated in Table 3. For H_2-He envelopes, we use the EOS of Saumon et al. (1995).

We do not employ thermal corrections in our model, but we can estimate their effect from the coefficients of thermal expansion. The volume thermal expansion coefficient at high pressures has been measured to be $2 - 3 \times 10^{-5}$ K^{-1} for iron (Boehler et al. 1990) and 4×10^{-5} K^{-1} for $MgSiO_3$ (Knittle et al. 1986). Taking 3×10^{-5} K^{-1} as an average, or a linear coefficient of 1×10^{-5} K^{-1}, and an internal temperature of 5,000 K, typical of Earth's core (Poirier 1994), we can estimate a thermal correction to the planetary radius of about 5%. However, the internal temperature may be significantly higher for larger planets.

Alternatively, we can find the total error produced by our code from an Earth-analog model. Specifically a 1-$M_\oplus$ planet model with an "Earth-like" composition produced by our code has a radius of 0.972 $R_\oplus$, an error of 2.8%. This includes the error introduced by thermal expansion compared with our zero-temperature model, the errors in the equations of state, and the error introduced by the simplifying assumption of a two-layer model. Since the EOS-induced errors are small for a 1-$M_\oplus$ planet, it is possible that thermal expansion is a significant contributor to this error.

We compare our mass-radius results for a simple iron core/$MgSiO_3$-mantle planet to those obtained by Seager et al. (2007), to determine the effect of any differences in the EOS. We test a pure $MgSiO_3$ composition, a 32.5% iron core mass fraction (CMF) ("Earth-like") composition, a 70% CMF ("Mercury-like") composition, and a pure iron composition for masses ranging from $0.5M_\oplus$ to $20M_\oplus$. We find agreement to within 1% in all cases, with the exception of pure iron planets, which differ by up to -2.23% for $20M_\oplus$. This is likely due to the effect on the EOS of the higher central pressures of iron planets. Planets of mass 10 $M_\oplus$ composed of pure iron, 70% iron, 32.5% iron, and pure $MgSiO_3$ (perovskite) have central pressures of 88 Mbar, 78 Mbar, 54 Mbar, and 18 Mbar, respectively.

As Figures 19 and 20 demonstrate, there can be slight differences between different EOS fits. Ambiguities are especially prominent in the 1 to 1000 Mbar pressure range, above pressures one can probe with constant-temperature experiments, but below where the Thomas-Fermi-Dirac EOS becomes applicable (Hemley et al. 1987). In order to investigate the effect of EOS ambiguities on a terrestrial planet model, we multiply the density for all pressures by a constant error factor. The resulting mass-radius curves for pure iron and pure silicate planets are given in Figure 21.

For a 10% swing in density at a given pressure (on the order of the differences between EOSs in Figure 20), we find changes in radius for pure $MgSiO_3$ planets of -3.5% (0.1 $M_\oplus$), -4.0% (1.0 $M_\oplus$), -4.6% (5.0 $M_\oplus$), -5.0% (10.0 $M_\oplus$), and -5.5% (20.0 $M_\oplus$). For pure iron planets, we find changes of -3.7% (0.1 $M_\oplus$), -4.4% (1.0 $M_\oplus$), -5.0% (5.0 $M_\oplus$), -5.3% (10.0 $M_\oplus$), and -6.4% (20.0 $M_\oplus$).

While most equations of state for a given material will agree on the low-pressure density (as it is easily measured), the differences between equations of state in the 1 to 1000 Mbar range could exceed 5%. Because of this, the ambiguities in radius we report are relevant to high-mass planets (without envelopes) and solid cores whose central pressures lie where the equation of state is ambiguous. In particular, the uncertainties in radius due to the equation of state are similar in magnitude to the change in radius caused by differentiation and different mantle material (e.g. silicates vs. silicon carbide), so more accurate equations of state are needed to distinguish these cases.

REFERENCES

Ahrens, T. J. 2000, Mineral Physics and Crystallography: A Handbook of Physical Constants (Washington, DC: American Geophysical Union)

Aleksandrov, I. V., Goncharov, A. F., Stishov, S. M., & Yakovenko, E. V. 1989, Soviet Journal of Experimental and Theoretical Physics Letters, 50, 127

Anderson, O., & Isaak, D. G. 2000, Am, Mineral, 85, 376

Anderson, O. L., Dubrovinsky, L., Saxena, S. K., & LeBihan, T. 2001, Geophys. Res. Lett., 28, 399

Anderson, O. L., Isaak, D. L., & Oda, H. 1991, J. Geophys. Res., 96, 18037

Baglin, A., Auvergne, M., Barge, P., Deleuil, M., Catala, C., Michel, E., Weiss, W., & The COROT Team. 2006, in ESA Special Publication, Vol. 1306, ESA Special Publication, ed. M. Fridlund, A. Baglin, J. Lochard, & L. Conroy, 33–+

Barclay, T., et al. 2013, Nature, 494, 452

Batalha, N. M., et al. 2011, Astrophys. J., 729, 27

—. 2013, ApJS, 204, 24

Batygin, K., Bodenheimer, P., & Laughlin, G. 2009, ApJ, 704, L49

Boehler, R., von Bargen, N., & Chopelas, A. 1990, J. Geophys. Res., 95, 21731

Borucki, W. J., et al. 2010, Science, 327, 977

Bouhifd, M. A., Andrault, D., Fiquet, G., & Richet, P. 1996, Geophys. Res. Lett., 23, 1143

Carter, J. A., Winn, J. N., Holman, M. J., Fabrycky, D., Berta, Z. K., Burke, C. J., & Nutzman, P. 2011, ApJ, 730, 82

Carter, J. A., et al. 2012, Science, 337, 556

Chandrasekhar, S. 1939, An introduction to the study of stellar structure, ed. Chandrasekhar, S.

Cochran, W. D., et al. 2011, ApJS, 197, 7

Crossfield, I. J. M., Barman, T., Hansen, B. M. S., & Howard, A. W. 2013, A&A, 559, A33
Dewaele, A., Loubeyre, P., Occelli, F., Mezouar, M., Dorogokupets, P. I., & Torrent, M. 2006, Physical Review Letters, 97, 215504
Dong, S., & Zhu, Z. 2013, ApJ, 778, 53
Dragomir, D., et al. 2013, ApJ, 772, L2
Duffy, T. S., Zha, C.-S., Downs, R. T., Mao, H.-K., & Hemley, R. J. 1995, Nature, 378, 170
Endl, M., et al. 2012, ApJ, 759, 19
Fei, Y., Mao, H.-K., & Hemley, R. J. 1993, J. Chem. Phys., 99, 5369
Fortney, J. J., Marley, M. S., & Barnes, J. W. 2007, Astrophys. J., 659, 1661
Gautier, III, T. N., et al. 2012, ApJ, 749, 15
Gilliland, R. L., et al. 2013, ApJ, 766, 40
Gillon, M., et al. 2012, VizieR Online Data Catalog, 353, 99028
Grasset, O., Schneider, J., & Sotin, C. 2009, ApJ, 693, 722
Haghighipour, N. 2011, ArXiv e-prints
Halliday, D., Resnick, R., & Walker, J. 2003, Fundamentals of Physics, ed. Halliday, D., Resnick, R., & Walker, J.
Hama, J., & Suito, K. 1996, Journal of Physics Condensed Matter, 8, 67
Hanfland, M., Beister, H., & Syassen, K. 1989, Phys. Rev. B, 39, 12598
Hartman, J. D., et al. 2011, ApJ, 728, 138
Hauck, S. A., et al. 2013, Journal of Geophysical Research (Planets), 118, 1204
Hemley, R. J., Jephcoat, A. P., Mao, H. K., Zha, C. S., Finger, L. W., & Cox, D. E. 1987, Nature, 330, 737
Hemley, R. J., Stixrude, L., Fei, Y., & Mao, H. K. 1992, in High Pressure Research: Applications to Earth and Planetary Sciences, ed. Y. Syono & M. H. Manghnani, Vol. 67 (AGU Monogr.), 183–189
Howard, A. W., et al. 2012, ApJS, 201, 15
Hubbard, W. B., Hattori, M. F., Burrows, A., Hubeny, I., & Sudarsky, D. 2007, Icarus, 187, 358
Jontof-Hutter, D., Lissauer, J. J., Rowe, J. F., & Fabrycky, D. C. 2013, ArXiv e-prints
Kavner, A., Duffy, T. S., & Shen, G. 2001, Earth and Planetary Science Letters, 185, 25
King, Jnr, H. E., & Prewitt, C. T. 1982, Acta Crystallographica Section B, 38, 1877
Knittle, E., & Jeanloz, R. 1987, Science, 235, 668
Knittle, E., Jeanloz, R., & Smith, G. L. 1986, Nature, 319, 214
Kunc, K., Loa, I., & Syassen, K. 2003, Phys. Rev. B, 68, 094107
Lide, D. R. 2005, Handbook of Chemistry and Physics (CRC Press, New York)
Lin, J.-F., Campbell, A. J., Heinz, D. L., & Shen, G. 2003, Journal of Geophysical Research (Solid Earth), 108, 2045
Lissauer, J. J., Hubickyj, O., D'Angelo, G., & Bodenheimer, P. 2009, Icarus, 199, 338
Lissauer, J. J., et al. 2011, Nature, 470, 53
Lopez, E. D., & Fortney, J. J. 2013, ArXiv e-prints
Lu, Y.-P., He, D.-W., Zhu, J., & Yang, X.-D. 2008, Physica B Condensed Matter, 403, 3543
Lyon, S. P., & Johnson, J. D. 1992, LA-UR-92-3407, LANL
Marcy, G. W., et al. 2014, ApJS, 210, 20
Marcy, G. W., et al. 2014, PNAS, in press
Masuda, K. 2014, ArXiv e-prints
Masuda, K., Hirano, T., Taruya, A., Nagasawa, M., & Suto, Y. 2013, ApJ, 778, 185
Moutou, C., et al. 2013, Icarus, 226, 1625
Nettelmann, N., Holst, B., Kietzmann, A., French, M., Redmer, R., & Blaschke, D. 2008, ApJ, 683, 1217
Ofir, A., Dreizler, S., Zechmeister, M., & Husser, T.-O. 2014, A&A, 561, A103
Olinger, B. 1977, in High Pressure Physics Research: Applications in Geophysics, ed. M. H. Manghnani & S. Akimoto (New York: Academic Press), 325–334
Pepe, F., et al. 2013, ArXiv e-prints
Poirier, J.-P. 1994, Academie des Science Paris Comptes Rendus Serie B Sciences Physiques, 318, 341
—. 2000, Introduction to the Physics of the Earth's Interior, ed. Poirier, J.-P.
Rafikov, R. R. 2011, ApJ, 727, 86
Rogers, L. A., Bodenheimer, P., Lissauer, J. J., & Seager, S. 2011, ApJ, 738, 59
Salpeter, E. E., & Zapolsky, H. S. 1967, Physical Review, 158, 876
Sanchis-Ojeda, R., et al. 2012, Nature, 487, 449
Saumon, D., Chabrier, G., & van Horn, H. M. 1995, Astrophys. J., Suppl. Ser., 99, 713
Seager, S., Kuchner, M., Hier-Majumder, C. A., & Militzer, B. 2007, Astrophys. J., 669, 1279
Sotin, C., Grasset, O., & Mocquet, A. 2007, Icarus, 191, 337
Speziale, S., Zha, C.-S., Duffy, T. S., Hemley, R. J., & Mao, H.-k. 2001, J. Geophys. Res., 106, 515
Steffen, J. H., et al. 2013, MNRAS, 428, 1077
Stevenson, D. J. 1982, Annual Review of Earth and Planetary Sciences, 10, 257
Stewart, S. T., & Ahrens, T. J. 2005, Journal of Geophysical Research (Planets), 110, E03005
Stixrude, L., & Lithgow-Bertelloni, C. 2005, Geophysical Journal International, 162, 610
Sun, T., Umemoto, K., Wu, Z., Zheng, J.-C., & Wentzcovitch, R. M. 2008, Phys. Rev. B, 78, 024304
Thompson, S. L. 1990, ANEOS–Analytic Equations of State for Shock Physics Codes, Sandia Natl. Lab. Doc. SAND89-2951
Tsuchiya, T., Tsuchiya, J., Umemoto, K., & Wentzcovitch, R. M. 2004, Earth and Planetary Science Letters, 224, 241
Uchida, T., Wang, Y., Rivers, M. L., & Sutton, S. R. 2001, J. Geophys. Res., 106, 21799
Vacher, P., Mocquet, A., & Sotin, C. 1998, Physics of the Earth and Planetary Interiors, 106, 275
Valencia, D., O'Connell, R. J., & Sasselov, D. 2006, Icarus, 181, 545
—. 2007b, Astrophys. J., 656, 545
Valencia, D., Sasselov, D. D., & O'Connell, R. J. 2007a, Astrophys. J., 665, 1413
Vinet, P., Rose, J. H., Ferrante, J., & Smith, J. R. 1989, Journal of Physics Condensed Matter, 1, 1941
Weiss, L. M., & Marcy, G. W. 2014, ApJ, 783, L6
Williams, Q., & Knittle, E. 1997, Physics of the Earth and Planetary Interiors, 100, 49
Wolanin, E., Pruzan, P., Chervin, J. C., Canny, B., Gauthier, M., Häusermann, D., & Hanfland, M. 1997, Phys. Rev. B, 56, 5781
Zapolsky, H. S., & Salpeter, E. E. 1969, Astrophys. J., 158, 809
Zhao, Y. X., & Spain, I. L. 1989, Phys. Rev. B, 40, 993

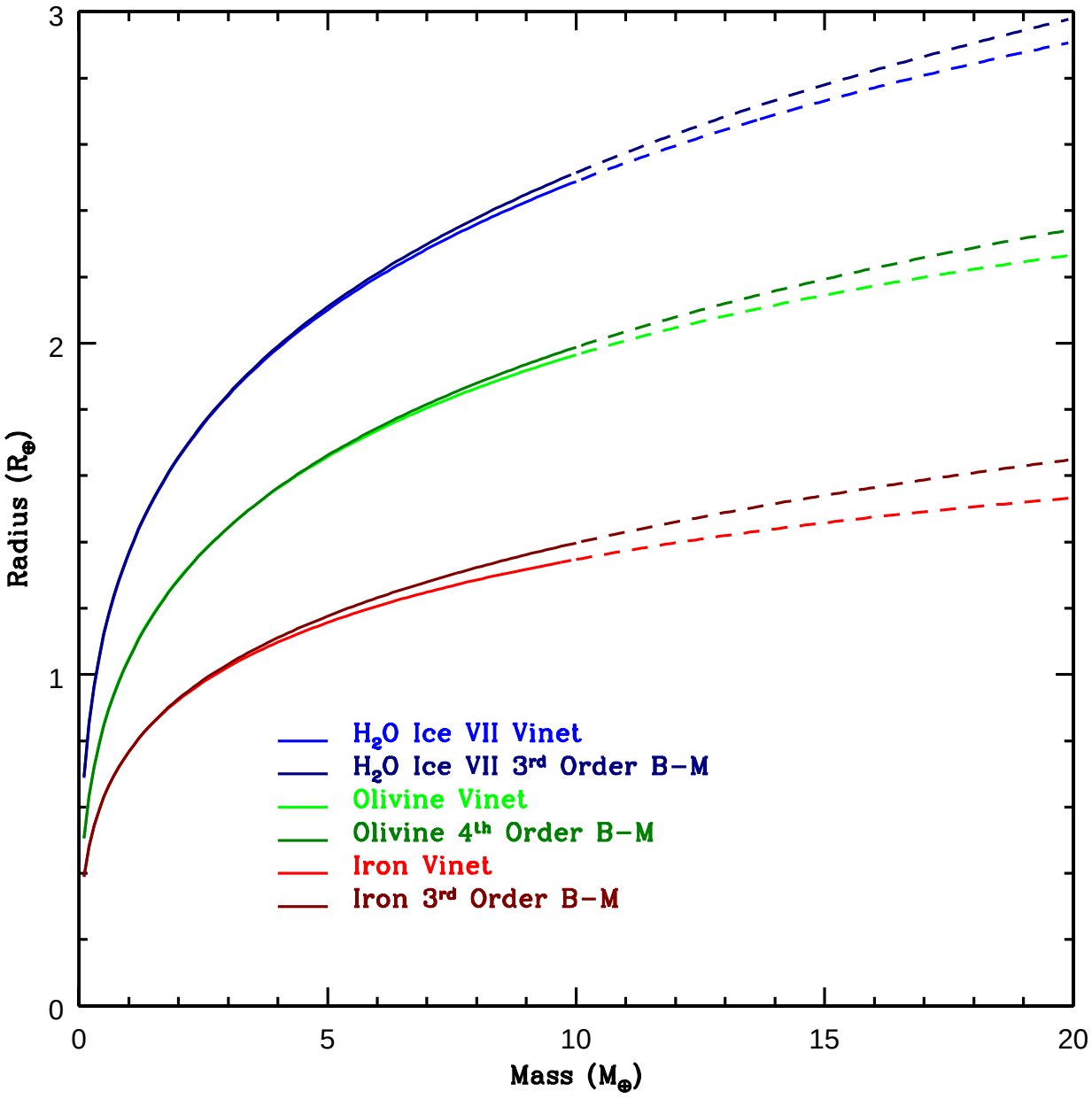

FIG. 19.— Comparison of mass-radius curves computed with Vinet and Birch-Murnaghan EOSs for water (in the form of Ice VII), Mg_2SiO_4 (olivine), and iron. The two EOS fits agree in the low-pressure limit where the uncompressed density dominates, but deviate at high pressures. For context, the EOS fits for olivine differ by only 0.2% for 1 Earth-mass planets, but differ increasingly as planet mass increases (to 6.8% for 20 Earth-mass planets).

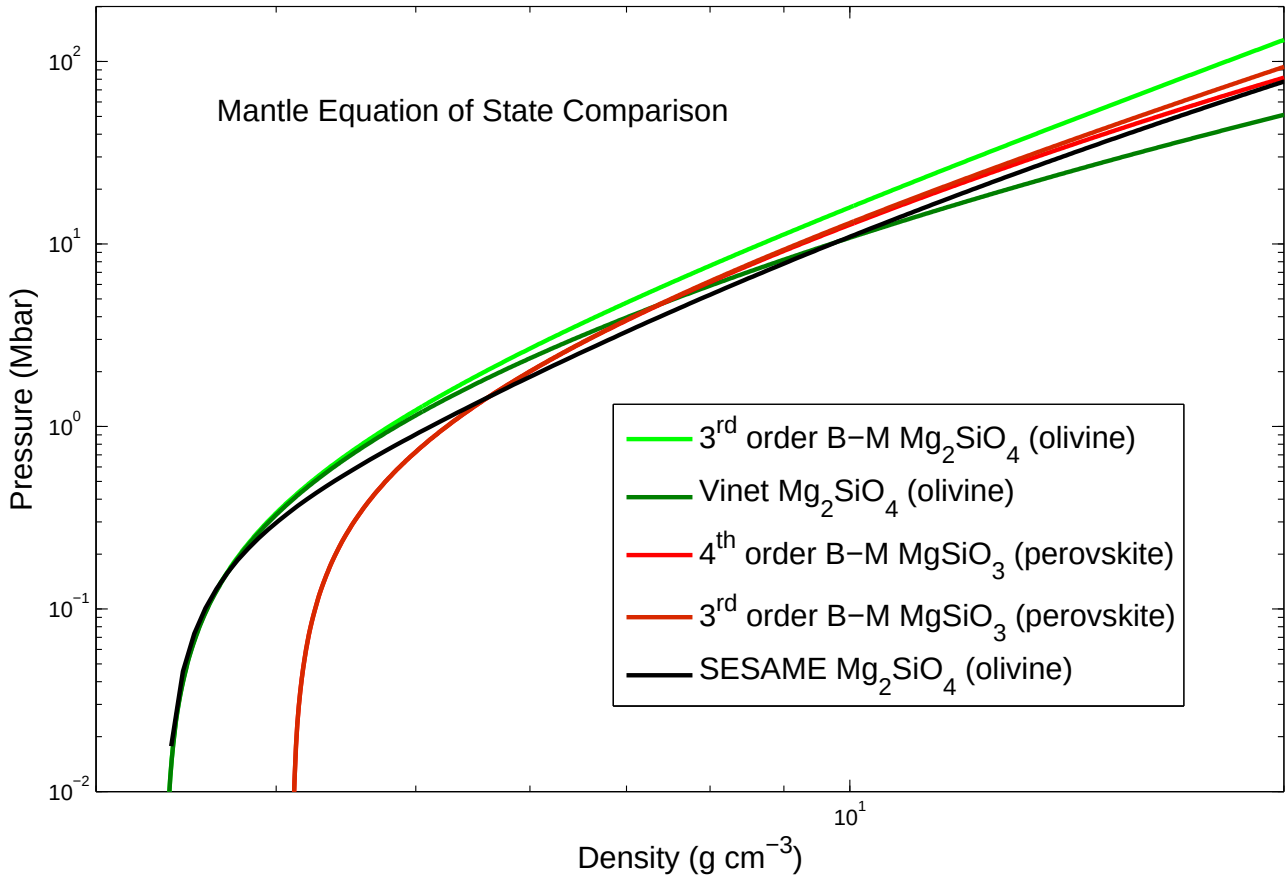

FIG. 20.— Comparison of various equations of state for mantle materials. At high pressures (>1 Mbar) the equations of state for the two materials become similar, with the greatest differences between the various equations of state occurring for Mg_2SiO_4 (olivine). This implies that for mantle materials at high pressures, the choice of material has a less significant effect than the choice of EOS fit. However, at pressures approaching zero, the uncompressed density dominates, making the choice of material far more significant than the choice of EOS fit at low pressures.

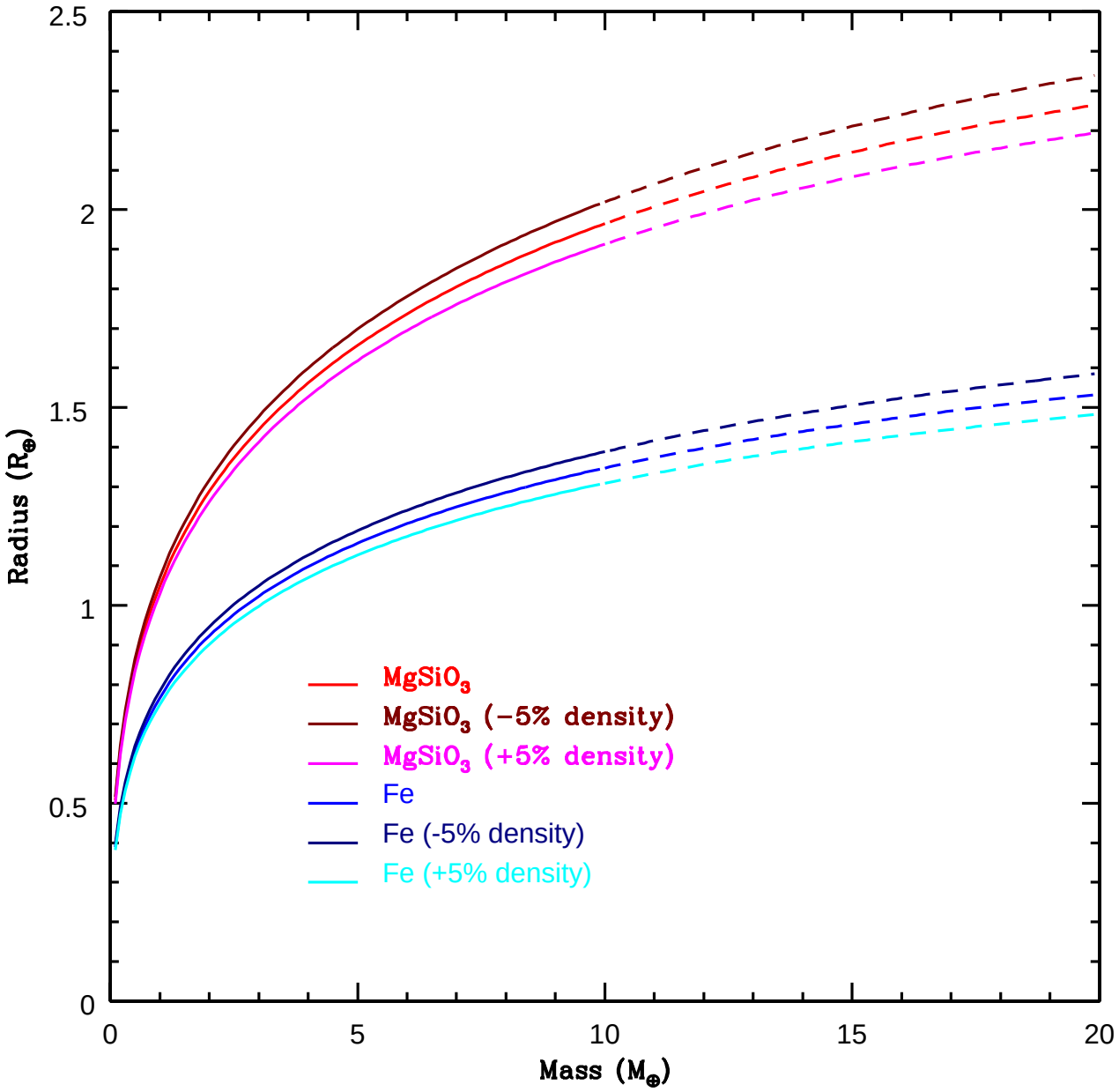

FIG. 21.— Mass-radius curves for pure iron and silicate planets. A proportional EOS error in density is applied to investigate the effects of EOS ambiguities on terrestrial planet models. For a 10% swing in density at a given pressure, we find changes in radius ranging from -3.5% for a silicate, 0.1-$M_\oplus$ planet to -6.4% for an iron, 20-$M_\oplus$ planet.

TABLE 5
EARTH-LIKE CORE/H_2-HE ENVELOPE PLANETS WITH $M_{env} = 0.1$ $M_\oplus$, $s = 6.0\,k_B/B$

Core Mass ($M_\oplus$)	Radius ($R_\oplus$)	Central Pressure (Mbar)	Central Density (g cm^{-3})
0.4	4.26148	1.97466	12.5530
0.6	3.47101	2.28146	13.5698
0.8	3.06142	3.66167	14.4290
1	2.79890	4.50292	15.1893
2	2.33196	8.82066	18.2349
3	2.21482	13.3997	20.6751
4	2.17903	18.2692	22.8259
5	2.17231	23.4375	24.8049
6	2.17681	28.9078	26.6708
7	2.18852	34.6839	28.4580
8	2.20358	40.7688	30.1884
9	2.21951	47.1661	31.8770
10	2.23497	53.1950	33.5349
12	2.26575	69.0382	36.7901
14	2.29493	84.0288	40.0016
16	2.32147	101.173	43.2015
18	2.34494	119.786	46.4135
20	2.36655	139.946	49.6562

TABLE 6
EARTH-LIKE CORE/H_2-HE ENVELOPE PLANETS WITH $M_c = 2$ $M_\oplus$, $s = 5.5\,k_B/B$

Envelope Mass ($M_\oplus$)	Radius ($R_\oplus$)	Central Pressure (Mbar)	Central Density (g cm^{-3})
0.00	1.18851	8.69496	18.1594
0.02	1.56409	8.73952	18.1862
0.04	1.73518	8.76965	18.2044
0.06	1.87084	8.79355	18.2187
0.08	1.99033	8.81374	18.2308
0.10	2.09529	8.83109	18.2412
0.20	2.52114	8.89454	18.2790
0.30	2.84728	8.93799	18.3049
0.40	3.11830	8.97101	18.3245
0.50	3.35079	8.99829	18.3407
0.60	3.55310	9.02147	18.3544
0.70	3.73529	9.04193	18.3665
0.80	3.89788	9.06027	18.3773
0.90	4.04563	9.07698	18.3872
1.00	4.18264	9.09255	18.3963
1.20	4.42436	9.12031	18.4127
1.40	4.63533	9.14551	18.4275
1.60	4.82146	9.16841	18.4409
1.80	4.98358	9.18966	18.4534

TABLE 7
EARTH-LIKE CORE/H_2-HE ENVELOPE PLANETS WITH $M_c = 2$ $M_\oplus$, $s = 6.0\,k_B/B$

Envelope Mass ($M_\oplus$)	Radius ($R_\oplus$)	Central Pressure (Mbar)	Central Density (g cm^{-3})
0.00	1.18851	8.69496	18.1594
0.02	1.67729	8.73677	18.1846
0.04	1.88652	8.76455	18.2013
0.06	1.97443	8.78670	18.2146
0.08	2.20039	8.80485	18.2255
0.10	2.33232	8.82073	18.2350
0.20	2.85687	8.87792	18.2691
0.30	3.25957	8.91662	18.2922
0.40	3.59448	8.94581	18.3095
0.50	3.87978	8.97001	18.3239
0.60	4.12971	8.99055	18.3361
0.70	4.34681	9.00852	18.3467
0.80	4.54684	9.04297	18.3565
0.90	4.72604	9.03955	18.3651
1.00	4.89030	9.05350	18.3733
1.20	5.17685	9.07834	18.3880
1.40	5.42263	9.10066	18.4011
1.60	5.63461	9.12127	18.4132
1.80	5.82015	9.14026	18.4244

TABLE 8
EARTH-LIKE CORE/H_2-HE ENVELOPE PLANETS WITH $M_c = 2$ $M_\oplus$, $s = 6.5\,k_B/B$

Envelope Mass ($M_\oplus$)	Radius ($R_\oplus$)	Central Pressure (Mbar)	Central Density (g cm^{-3})
0.00	1.18851	8.69496	18.1594
0.02	1.84538	8.73323	18.1825
0.04	2.12095	8.75821	18.1975
0.06	2.34125	8.77764	18.2092
0.08	2.53227	8.79358	18.2187
0.10	2.70473	8.80722	18.2269
0.20	3.40678	8.85628	18.2562
0.30	3.94117	8.88858	18.2755
0.40	4.38415	8.91308	18.2901
0.50	4.76993	8.93324	18.3021
0.60	5.10259	8.95047	18.3123
0.70	5.39890	8.96549	18.3212
0.80	5.66089	8.97905	18.3293
0.90	5.89601	8.99134	18.3366
1.00	6.10857	9.00277	18.3422
1.20	6.47809	9.02340	18.3555
1.40	6.78834	9.04236	18.3667

TABLE 9
EARTH-LIKE CORE/H_2-HE ENVELOPE PLANETS WITH $M_c = 5$ $M_\oplus$, $s = 6.0\,k_B/B$

Envelope Mass ($M_\oplus$)	Radius ($R_\oplus$)	Central Pressure (Mbar)	Central Density (g cm^{-3})
0.00	1.52092	23.2071	24.7228
0.02	1.80841	23.2701	24.7445
0.04	1.92515	23.3202	24.7626
0.06	2.01793	23.3631	24.7781
0.08	2.09911	23.4022	24.7922
0.10	2.17720	23.4374	24.8049
0.20	2.47107	23.5808	24.8565
0.30	2.70888	23.6902	24.8957
0.40	2.91421	23.7796	24.9277
0.50	3.09611	23.8562	24.9550
0.60	3.26045	23.9224	24.9786
0.70	3.41082	23.9813	24.9996
0.80	3.55018	24.0346	25.0186
0.90	3.67956	24.0840	25.0361
1.00	3.80286	24.1288	25.0520
1.20	4.02328	24.2093	25.0806
1.40	4.22312	24.2808	25.1059
1.60	4.40458	24.3449	25.1285
1.80	4.57070	24.4041	25.1495
2.00	4.72406	24.4582	25.1685
2.50	5.06239	24.5797	25.2113
3.00	5.34830	24.6854	25.2484
3.50	5.59620	24.7809	25.2819
4.00	5.83033	24.8764	25.3153
4.50	6.00929	24.9518	25.3416

TABLE 10
EARTH-LIKE CORE/H_2-HE ENVELOPE PLANETS WITH $M_c = 10$ $M_\oplus$, $s = 6.0\,k_B/B$

Envelope Mass ($M_\oplus$)	Radius ($R_\oplus$)	Central Pressure (Mbar)	Central Density (g cm^{-3})
0.00	1.79615	53.5130	33.4467
0.02	1.99228	53.6051	33.4688
0.04	2.07032	53.6835	33.4876
0.06	2.13342	53.7542	33.5046
0.08	2.18642	53.8190	33.5201
0.10	2.23596	53.8813	33.5350
0.20	2.43488	54.1477	33.5987
0.30	2.59648	54.3693	33.6515
0.40	2.73667	54.5604	33.6971
0.50	2.86268	54.7313	33.7377
0.60	2.97828	54.8846	33.7741
0.70	3.08500	55.0238	33.8071
0.80	3.18559	55.1530	33.8377
0.90	3.28040	55.2727	33.8660
1.00	3.36982	55.3828	33.8920
1.20	3.53525	55.5862	33.9400
1.40	3.69025	55.7704	33.9834
1.60	3.83086	55.9349	34.0222
1.80	3.96291	56.0866	34.0578
2.00	4.08644	56.2271	34.0908
2.50	4.36723	56.5416	34.1644
3.00	4.61361	56.8150	34.2283
3.50	4.83412	57.0578	34.2850
4.00	5.03420	57.2804	34.3368
4.50	5.21535	57.4825	34.3837
5.00	5.38451	57.6730	34.4279
6.00	5.68357	58.0220	34.5087
7.00	5.94431	58.3358	34.5811
8.00	6.17595	58.6298	34.6488

TABLE 11
PURE $MgSiO_3$ (PEROVSKITE) PLANETS

Mass ($M_\oplus$)	Radius ($R_\oplus$)	Central Pressure (Mbar)	Central Density (g cm^{-3})	Moment of Inertia Coefficient	Love Number
0.2	0.634704	0.44969	4.66933	0.393552	1.44028
0.4	0.791132	0.76609	5.00284	0.390316	1.41086
0.6	0.897857	1.06129	5.27594	0.387828	1.38849
0.8	0.980917	1.34800	5.51649	0.385748	1.36996
1	1.04968	1.63112	5.73586	0.383937	1.35394
2	1.28797	3.05157	6.66347	0.377068	1.29423
3	1.44433	4.53165	7.45104	0.372061	1.25173
4	1.56222	6.09528	8.17135	0.368002	1.21790
5	1.65714	7.75175	8.85318	0.364533	1.18944
6	1.73659	9.50646	9.51142	0.361472	1.16466
7	1.80482	11.3635	10.1551	0.358711	1.14258
8	1.86449	13.3270	10.7901	0.356182	1.12257
9	1.91740	15.4003	11.4208	0.353835	1.10420
10	1.96480	17.5872	12.0502	0.351639	1.08716
12	2.04659	22.3176	13.3149	0.347598	1.05624
14	2.11495	27.5538	14.5999	0.343920	1.02854
16	2.17308	33.3339	15.9166	0.340510	1.00325
18	2.22312	39.7017	17.2748	0.337307	0.979828
20	2.26653	46.7077	18.6833	0.334268	0.957907

TABLE 12
32.5% IRON / 67.5% $MgSiO_3$ (PEROVSKITE) DIFFERENTIATED PLANETS

Mass ($M_\oplus$)	Radius ($R_\oplus$)	Central Pressure (Mbar)	Central Density (g cm^{-3})	Moment of Inertia Coefficient	Love Number
0.2	0.592384	1.08997	11.2072	0.343216	1.023290
0.4	0.736224	1.94664	12.5157	0.338446	0.988125
0.6	0.833926	2.77697	13.5207	0.335116	0.963997
0.8	0.909741	3.60223	14.3719	0.332500	0.945281
1.0	0.972372	4.43009	15.1266	0.330321	0.929855
2	1.18850	8.69494	18.1594	0.322687	0.876945
3	1.32962	13.2340	20.5953	0.317587	0.842566
4	1.43571	18.0696	22.7440	0.313667	0.816658
5	1.52093	23.2070	24.7217	0.310443	0.795674
6	1.59214	28.6485	26.5866	0.307682	0.777946
7	1.65321	34.3970	28.3729	0.305251	0.762511
8	1.70657	40.4541	30.1021	0.303072	0.748814
9	1.75383	46.8249	31.7898	0.301086	0.736450
10	1.79616	53.5130	33.4467	0.299257	0.725152
12	1.86914	67.8618	36.6994	0.295967	0.705063
14	1.93012	83.5511	39.9084	0.293043	0.687452
16	1.98200	100.637	43.1054	0.290395	0.671695
18	2.02670	119.191	46.3144	0.287957	0.657353
20	2.06553	139.285	49.5533	0.285685	0.644125

TABLE 13
32.5% Iron / 67.5% $MgSiO_3$ (perovskite) Undifferentiated Planets

Mass ($M_\oplus$)	Radius ($R_\oplus$)	Central Pressure (Mbar)	Central Density (g cm^{-3})	Moment of Inertia Coefficient	Love Number
0.2	0.593662	0.596268	5.82786	0.391631	1.42277
0.4	0.737793	1.03360	6.33721	0.387721	1.38754
0.6	0.835511	1.44955	6.75061	0.384795	1.36151
0.8	0.911201	1.85902	7.11316	0.382392	1.34036
1	0.973627	2.26762	7.44304	0.380326	1.32234
2	1.18822	4.36307	8.83494	0.372674	1.25688
3	1.32751	6.60057	10.0176	0.367235	1.21157
4	1.43167	9.00490	11.1022	0.362889	1.17609
5	1.51499	11.5858	12.1321	0.359210	1.14655
6	1.58431	14.3501	13.1295	0.355986	1.12103
7	1.64351	17.3037	14.1081	0.353093	1.09842
8	1.69501	20.4523	15.0765	0.350453	1.07803
9	1.74045	23.8027	16.0411	0.348012	1.05938
10	1.78097	27.3617	17.0068	0.345733	1.04214
12	1.85037	35.1346	18.9558	0.341553	1.01095
14	1.90784	43.8386	20.9471	0.337757	0.983102
16	1.95624	53.5474	22.9986	0.334245	0.957743
18	1.99745	64.3474	25.1257	0.330952	0.934310
20	2.03281	76.3381	27.3427	0.327830	0.912400

TABLE 14
70% Iron / 30% $MgSiO_3$ (perovskite) Differentiated Planets

Mass ($M_\oplus$)	Radius ($R_\oplus$)	Central Pressure (Mbar)	Central Density (g cm^{-3})	Moment of Inertia Coefficient	Love Number
0.2	0.535687	1.39506	11.7182	0.331929	0.941222
0.4	0.662772	2.54306	13.2557	0.325122	0.893634
0.6	0.748595	3.67582	14.4425	0.320532	0.862322
0.8	0.814977	4.81495	15.4518	0.317012	0.838737
1	0.869685	5.96775	16.3500	0.314140	0.819759
2	1.05786	12.0087	19.9881	0.304481	0.757654
3	1.18039	18.5516	22.9409	0.298355	0.719616
4	1.27243	25.6011	25.5667	0.293811	0.692052
5	1.34640	33.1514	27.9993	0.290172	0.670378
6	1.40823	41.2004	30.3062	0.287125	0.652494
7	1.46131	49.7471	32.5268	0.284494	0.637243
8	1.50776	58.7933	34.6864	0.282170	0.623922
9	1.54895	68.3429	36.8026	0.280086	0.612089
10	1.58589	78.4005	38.8879	0.278191	0.601427
12	1.64978	100.070	43.0034	0.274837	0.582766
14	1.70339	123.870	47.0883	0.271918	0.566756
16	1.74922	149.882	51.1807	0.269319	0.552668
18	1.78893	178.211	55.3085	0.266962	0.540038
20	1.82366	208.966	59.4937	0.264799	0.528556

TABLE 15
70% Iron / 30% $MgSiO_3$ (perovskite) Undifferentiated Planets

Mass ($M_\oplus$)	Radius ($R_\oplus$)	Central Pressure (Mbar)	Central Density (g cm^{-3})	Moment of Inertia Coefficient	Love Number
0.2	0.537303	0.914989	8.15393	0.388075	1.39070
0.4	0.664291	1.63148	9.06921	0.383210	1.34754
0.6	0.749565	2.33087	9.79947	0.379740	1.31726
0.8	0.815181	3.03122	10.4338	0.376976	1.29344
1	0.869019	3.73887	11.0074	0.374654	1.27363
2	1.05228	7.45597	13.4028	0.366385	1.20459
3	1.16984	11.5200	15.4184	0.360753	1.15888
4	1.25710	15.9491	17.2568	0.356359	1.12397
5	1.32649	20.7482	18.9951	0.352702	1.09539
6	1.38396	25.9242	20.6731	0.349537	1.07101
7	1.43288	31.4829	22.3140	0.346723	1.04961
8	1.47531	37.4317	23.9330	0.344175	1.03045
9	1.51264	43.7801	25.5410	0.341835	1.01304
10	1.54585	50.5397	27.1464	0.339662	0.997022
12	1.60261	65.3367	30.3725	0.335705	0.968238
14	1.64946	81.9292	33.6493	0.332143	0.942742
16	1.68884	100.440	37.0047	0.328869	0.919659
18	1.72233	121.008	40.4615	0.325821	0.898451
20	1.75106	143.796	44.0398	0.322946	0.878711

TABLE 16
Pure Iron Planets

Mass ($M_\oplus$)	Radius ($R_\oplus$)	Central Pressure (Mbar)	Central Density (g cm^{-3})	Moment of Inertia Coefficient	Love Number
0.2	0.481284	1.47742	11.8462	0.383411	1.34930
0.4	0.591383	2.71052	13.4467	0.377909	1.30145
0.6	0.664753	3.93539	14.6857	0.374237	1.27009
0.8	0.720967	5.17286	15.7419	0.371432	1.24645
1	0.766975	6.42967	16.6836	0.369141	1.22734
2	0.923092	13.0654	20.5136	0.361371	1.16385
3	1.02317	20.3131	23.6389	0.356330	1.12373
4	1.09763	28.1668	26.4291	0.352498	1.09380
5	1.15705	36.6171	29.0228	0.349359	1.06965
6	1.20647	45.6585	31.4895	0.346670	1.04921
7	1.24872	55.2906	33.8702	0.344303	1.03140
8	1.28555	65.5144	36.1910	0.342171	1.01552
9	1.31813	76.3373	38.4707	0.340226	1.00116
10	1.34727	87.7620	40.7217	0.338425	0.987969
12	1.39751	112.461	45.1776	0.335165	0.964350
14	1.43952	139.698	49.6177	0.332246	0.943477
16	1.47532	169.583	54.0822	0.329581	0.924650
18	1.50626	202.237	58.6007	0.327107	0.907365
20	1.53329	237.809	63.1980	0.324781	0.891285